Deterministic and stochastic rules of branching govern dendrite morphogenesis of sensory neurons

Amrutha Palavalli[1], Nicolás Tizón-Escamilla[2], Jean-François Rupprecht[2*] and Thomas Lecuit[1,3*]

1. Aix Marseille Université & CNRS, IBDM - UMR7288 & Turing Centre for Living Systems Campus de Luminy Case 907, 13288, Marseille, France
2. Aix-Marseille Université, Université de Toulon, CNRS, CPT, Turing Centre for Living Systems, Marseille, France.
3. Collège de France, 11 Place Marcelin Berthelot, 75005 Paris.

Correspondance : thomas.lecuit@univ-amu.fr
jean-francois.rupprecht@cpt.univ-mrs.fr

Abstract

Dendrite morphology is necessary for the correct integration of inputs that neurons receive. The branching mechanisms allowing neurons to acquire their type-specific morphology remain unclear. Classically, axon and dendrite patterns were shown to be guided by molecules providing deterministic cues. However, the extent to which deterministic and stochastic mechanisms, based upon purely statistical bias, contribute to the emergence of dendrite shape is largely unknown. We address this issue using the *Drosophila* class I vpda multi-dendritic neurons. Detailed quantitative analysis of vpda dendrite morphogenesis indicates that the primary branch grows very robustly in a fixed direction while secondary branch numbers and lengths showed fluctuations characteristic of stochastic systems. Live tracking dendrites and computational modeling revealed how neuron shape emerges from few local statistical parameters of branch dynamics. We report key opposing aspects of how tree architecture feedbacks on the local probability of branch shrinkage. Child branches promote stabilization of parent branches while self-repulsion promotes shrinkage. Finally, we show that self-repulsion, mediated by the adhesion molecule Dscam1, indirectly patterns the growth of secondary branches by spatially restricting their direction of stable growth perpendicular to the primary branch. Thus, the stochastic nature of secondary branch dynamics and the existence of geometric feedback emphasizes the importance of self-organization in neuronal dendrite morphogenesis.

Introduction

Dendrites are neuronal processes specialized to receive information. Neuronal subtypes have strikingly different arborization patterns. Dendrite patterns depend on several factors like the number and types of synaptic or sensory inputs received by the neuron or the geometry and size of the receptive fields. Failure to establish proper branching patterns leads to various neurodevelopmental disorders [1].

In general, dendrite morphogenesis follows a set of consecutive steps, which include (i) dendrite initiation, (ii) outgrowth (iii) branching and maturation (iv) establishment of boundaries and sometimes, arbor remodeling [2,3]. Every step requires extensive regulation by cell intrinsic cues as well as extrinsic cues.

Dendrite morphology is regulated cell-intrinsically by transcription factors [4–8], cytoskeletal regulators [9–15], components of endocytic pathway [16–18] and secretory pathway [19,20] all of which have been shown to either promote or reduce dendrite branching.

Extrinsic cues include, long-range diffusible secreted factors that are classically involved in axon guidance like Semaphorins [21] , Slits [22–24] and Netrins [25–27] also promote or restrict dendrite branching. Contact mediated, short range cues like cell adhesion molecules, adhesion GPCRs guide branch points [28], restrict branching [29] and maintain dendrites in a 2D plane [30]. Neuronal activity also refines arbor morphology by increasing or decreasing branching density [31,32]. Though much is known about the molecules regulating dendrite branching, how they govern the neuron-specific arborization patterns remains unclear. Indeed, most molecules tend to increase or decrease branching density without significantly affecting arborization patterns.

Two modes of branching morphogenesis have emerged from studying other branched organ systems [33–35]. The first one is deterministic, where systems have highly stereotyped branching patterns as described in the mouse lung [36] and *Drosophila* tracheal system [37]. Branching is orchestrated by patterned cues such as *Drosophila* FGF, which is expressed in clusters of cells surrounding the tracheal sacs at specific positions and instructs the branch points of the primary bud[37]. The dendrites of the *C. elegans* PVD neuron represent an extreme example of deterministic patterning in the neuronal system. The branch points in the complex menorah-like PVD dendrites are almost exclusively determined by patterned cues in the epidermis[28,38–40]. The second mode of branching is self-organized, wherein final morphology emerges from statistical features of branch dynamics and local interactions between growing tips. This results in stochastic branch patterns as described in mammary glands[34]. Although extrinsically derived FGF promotes branching in this system, no patterned cue has been identified that could potentially guide branching[41,42]. Mammary gland branching can be fully recapitulated by a model that accounts for local parameters such as tip elongation rate, branching rate and mode of tip termination[34]. Thus, branching morphogenesis of the mammary gland follows a stochastic, self-organized scheme and does not seem to require extrinsically patterned cues.

In neuronal systems, cell fate has traditionally been thought to be achieved deterministically by specific regulatory genes[43,44] but neuronal connectivity is refined by an activity-dependent, self-organization[45]. The overall shapes of homologous neurons are constant but their finer details are not[46,47]. Thus we wanted to further investigate the relative contribution of deterministic and self-organized mechanisms in establishing dendrite patterns.

The *Drosophila melanogaster* multi dendritic-dendritic arborization (md-da) neurons are the model of choice to address this question. Md-da neurons are part of the peripheral nervous system and are involved in somatosensation. They are divided into four distinct morphological classes in an increasing order of dendritic complexity. They exhibit stereotyped dendritic structures identifiable across animals and are restricted in a 2-D space beneath the epidermis [48–51]. Md-da neurons have been extensively used to study dendrite morphogenesis, especially class I and class IV neurons which exhibit the simplest and most complex morphologies respectively [6,8,52,53]. However, most studies were based on fixed imaging and have focused on late developmental stages, after the establishment of the typical dendritic morphology of the four neuronal classes.

In this study, we use high-resolution live imaging to quantitatively describe morphogenesis of class I vpda neuron. We show that the primary dendrites grow deterministically while secondary dendrite patterning is stochastic. Additionally, our computational model and Dscam1 data shows that self-repulsion patterns secondary dendrites by preferentially stabilizing them orthogonally from the primary dendrite giving the class I neurons their characteristic morphology.

Results

Class I vpda neuron shape is established during embryogenesis

To understand how class I specific dendrite morphology is achieved; we first investigated when final morphology of the dendritic arbor is established. The vpda neuron has one large primary dendrite that projects dorsally and another small primary branch on the ventral side. Secondary dendrites project outwards from the side of the primary dendrites giving vpda neurons their characteristic “bottle brush” morphology. Our study focused on the dorsal dendrite of the vpda neuron.

Dendrite morphology was analyzed at 4 developmental time points i.e. late embryogenesis, (E17, 19±2 hours After Egg Laying, or h AEL), 1st instar (L1, 24±3h AEL), 2nd instar (L2, 48±3h AEL) and 3rd instar (L3, 72±3h AEL). Neurons were labeled with UAS-mCD8::GFP, expressed by the neuronal class I specific driver 2-21gal4 [5]. We observed a qualitative enlargement of ventral vpda neurons over time that correlated with the growth of the organism (Figure 1A). To confirm this, we developed tools to quantitatively describe dendrite morphology. Vpda neuron dendrites were segmented and classified into primary, secondary, tertiary and quaternary branches (Schematic Figure 1A and Figure S1A-C). The branch numbers for each order of complexity were first measured. On average, 15-17 secondary branches emerged from the primary branch across the four developmental time points showing no statistically significant changes occurred during development (Figure 1B). The primary and secondary branches made up the bulk of the dendrite length (84.6% on average) at L3. The tertiary and quaternary branches made up, on average, 15.4% of the total dendrite length at L3 (Figure S1D) , and showed some changes during development but did not significantly alter the global dendrite pattern.

The total dendrite lengths made up by the primary, secondary, tertiary and quaternary branches also did not vary greatly across all 4 developmental stages (Figure S1D). Thus, the core morphology of vpda neurons dendrites is established in the embryo. Consistent with this, the relative distance between secondary branches did not change over time (Figure 1C), confirming that the dendrite pattern scales isometrically in size as the larva grows.

Thus, we set out to image dendrite morphogenesis in living embryos. Using a novel imaging setup we obtained movies covering complete dendrite morphogenesis (Video 1). These movies reveal 3 phases in vpda neuron morphogenesis: *(i) Primary dendrite formation*: Between 13-15h AEL, vpda neurons extend a single and stable primary dendrite towards the dorsal region of the embryo (Video 2). *(ii) Secondary branch initiation and elongation:* After ~15h AEL, flat lamellipodia-like membrane protrusions appeared at the distal tip of the primary dendrite (Figure 1D (i), (ii)). At ~17h AEL, numerous, small and dynamic protrusions that constantly extended and retracted appeared everywhere along the primary dendrite (Figure 1D (iii)). These dynamic protrusions were termed secondary extensions to distinguish them from stable secondary branches observed at later stages. On average 28.2±6.4 secondary extensions were present at 17h AEL (Figure 1E). Over the next 3-4 hours these extensions elongated at a rate of ~1µm/hour (Figure 1F). The growth of secondary extensions was accompanied by the emergence of dynamic protrusions branching off from secondary extensions, termed tertiary extensions. *(iii) Secondary branch stabilization:* After 20h AEL the dendritic structure became markedly less dynamic and secondary extension lengths (6±1.2µm) and numbers (17.6±3) stabilized at 22h AEL (Figure 1E-F). On average 62.3% of the initial secondary extensions were stabilized as secondary dendrites (Figure 1E).

The number of tertiary extensions dropped as the secondary extensions stabilized into secondary dendrites (Figure 1F-G). This number is even lower at later L1 (Figure 1B). Unlike secondary extensions no drastic change in tertiary extension lengths was observed over time (Figure 1H).

In summary, the primary branch grows dorsally in a straightforward manner followed by the emergence of dynamic secondary extensions undergoing repeated cycles of extension and retraction until stabilization of a subset of branches. Our observations reveal striking differences in the mode of development of the primary and secondary dendrites.

Growth of the primary dendrites is deterministic

Vpda neurons consistently form single dorsal primary dendrites that extend towards the dorsal region of the embryo (Figure 2A, Video 2). This reproducible growth pattern suggested a stringent control of primary dendrite number and orientation and hence deterministic growth.

When E-cadherin was co-expressed with the neurons to label the overlying epithelial cells, the primary dendrite coincided with the cadherin signal in 70% of the cases (17/24) (Figure 2B). Interestingly, even when the primary dendrite did not coincide with cadherin signal, it tracked parallel to these cell boundaries (Figure S2A). This hinted at the presence of a cue guiding the primary dendrite.

To assess the robustness of primary dendrite development, we mechanically perturbed growth by focusing an infrared laser to a point on the primary dendrite to cut a part of it at ~16h AEL and subsequently observed its recovery. We hypothesized that the dendrite would not be able to maintain growing dorsally as the guidance cue may be lost, since the ablation was carried out at a time after the completion of primary dendrite development. However, in all examined cases (n=15), ablated primary dendrites recovered and continued to grow dorsally (Figure 2C, Video3). This suggested that a persistent cue guided the primary dendrite. Together, these observations support the idea that primary dendrite number and orientation are defined deterministically.

Morphogenesis of the secondary dendrites is stochastic

Secondary branch growth was much more dynamic than primary branch growth (Figure 1). We also observed a higher variation in numbers and orientation of secondary branches. These observations argued against strictly deterministic growth. We therefore further investigated secondary dendrite growth properties.

At L3, secondary branch numbers ranged from 10 to 25 per neuron (mean 17± 3)(Figure 1B). This is consistent with stochastic systems where branching features are variable but distributed around a peak when analyzed statistically. However, this variation could reflect intersegment variability as neurons from all the abdominal hemi-segments were analyzed. Thus, we pooled data from larval dendrites of the same abdominal segment (A3) (Figure 3A). Secondary branch numbers ranged from 11-24 with a peak at 18±2.6 (Figure 3B), similar to Figure 1B.

However, this observed variation could also be an outcome of age variability between larvae. Hence, we compared dendrites from the left and right A3 hemi-segment of the same larva. The difference in secondary branch number between the left-right pairs (Figure 3C) ranged from -7 to 7 with a mean difference of -1±3.6 between the pairs indicating a high variability of branch number. Thus, secondary branch numbers are not tightly controlled but rather a result of stochastic differences arising during morphogenesis.

Interestingly, the variability of secondary branches between A2 and A3 segments on the left had similar distributions to left-right differences (Figure S2 B-D), further supporting that intersegment variation is mainly due to stochastic processes.

Further, we measured primary and secondary branch lengths at ~24h AEL. Primary branch lengths varied by 10.6% of the mean (Figure 3D) while for secondary branches variability was 57.7% (Figure 3E), further supporting the idea that primary branch growth is deterministic while secondary branch development is stochastic.

We then imaged growth at a higher temporal resolution (every 30sec) (Video 4). In contrast to the unidirectional growth of primary dendrites (Figure 2A), secondary and tertiary extensions alternated between phases of extension and retraction and, in doing so frequently changed direction (Figure 3F (i), Figure 3G-I). Further, secondary and tertiary extensions retracted upon contact with neighboring extensions, (Figure 3F (ii)); or self-repulsed. Growth rates of the secondary extensions also progressively reduced in time, particularly between 17h and 20h AEL. (Figure 3J).

In summary, secondary branch numbers arose stochastically from an initial higher number of dynamic extensions that self-repulse. This led us to explore how reproducible branching patterns emerge from the stochastic branch dynamics using a computational model.

A computational model of dendrite branching

Typical class I morphology is characterized by relatively low branch densities (total dendrite length per unit area is 0.0104 /µm) and smaller dendritic fields compared to other morphological classes such as class IV neurons (total dendrite length per unit area is 0.07/µm)[54].To identify key mechanisms responsible for dendrite patterning, we developed a computational model for stochastic branching to simulate secondary dendrite morphogenesis.

In our two-dimensional model (Figure 4A), extensions were modeled as polymers that grow (extend) and shrink (retract). We began with a fully formed primary dendrite (length $L_1 = 30$µm), which remained unaltered during the simulation. This corresponds to the neuron at ~15h AEL *in vivo*. New secondary extensions branch from the side of the primary dendrite at a rate λ_1. At a simulation time $t = 16$h AEL, tertiary (respectively quaternary) extensions emerge from the sides of pre-existing secondary (resp. tertiary) extensions at rates λ_2 (resp. λ_3). Once an extension appears, it either polymerizes (i.e. grows) or depolymerizes (i.e. shrinks) with growth or shrink velocities $v_{(2,3,4),on}$ and $v_{(2,3,4),off}$, where subscript number represents the order of complexity of the extension, and a persistence length l_p. An extension can spontaneously switch from a polymerizing to depolymerizing state (or *vice versa*) with a rate k_{off} (or k_{on} respectively). To complete this model, we introduced a contact-induced depolymerization or 'self-repulsion' as observed *in vivo* (Figure 3F(*ii*)). When a polymerizing extension encounters a neighboring dendrite it stops growing and shrinks with a probability p_{off}. Unless otherwise stated, we set $p_{off} = 1$, implying that extensions will always retract upon contact with neighbors.

We explored constitutive parameters of the model and found that a range of different dendrite morphologies can be described using this computational scheme. We observed that branching rates (λ), growth rates (v) and the ratio of spontaneous switching rates, $r = k_{on}/k_{off}$ played a fundamental role in dendrite architecture. Higher growth rates resulted in dendrites with larger dendritic field areas and longer branches (Figure 4C). On the other hand, increasing branching rates, increased branch numbers (Figure S3A,D). The ratio of spontaneous switching rates r had the highest impact on neuron morphology. For any value of both branching and growth rates, we could account for the wide phenomenology described by this model by simply changing the value of r. For low r values (i.e. higher probability of switching to a depolymerizing state) only a few short secondary extensions survived to final stages. For intermediate r values, moderate branch densities emerged, similar to class I dendrites. Finally, for values of r close or equal to 1, we obtained dendrites with very high densities and very large total areas (Figure 4C). This qualitative trend was observed irrespective of both growth and branching rates (Figure 4C,S3A,B).

However, despite an extensive parameter exploration, we were unable to find quantitative agreements between *in vivo* and simulated branches; the time evolution of branch number in simulated dendrites consistently deviated from *in vivo* values (Figure S3C,D, Figure 4E-F (blue lines)). Considering that *in vivo,* secondary branch dynamics slows down over time (Figure 3G-J), we incorporated a progressive decay of all dynamic parameters or an "aging factor". We reduced the rates of growth, branching and switching over time with differing intensities over time. By varying the aging intensity and kinetics, we obtained arborization patterns that ranged from being barely affected with highly active dendrites (for small aging factors) to dendrites that nearly froze at early stages exhibiting low-density arborization patterns (for high aging factors). Additionally, larger switching ratios required more intense aging factors in order to obtain branch numbers and lengths consistent with *in vivo* observations at intermediate and final time points (Figure 4D,F, S3E). To explore this, we chose two parameter sets (or Aging Protocols, AP), with switching ratios $r = 0.75$ (AP1) and $r = 1$ (AP2) (Figure 4D). The resulting branch numbers and lengths were consistent with *in vivo* observations for both protocols (Figure 4E-F (red lines), Figure S3F-G). Notably, for AP1 growth velocity was set to 0.62µm/min, in accordance with *in vivo* measurements (Figure 3J, Video5).

Thus, our computational model predicts the emergence of a range of possible dendrite morphologies from a few local statistical features of branch dynamics. For a wide subset of the parameter space, the combination of all the different elements of the model lead to arborization patterns consistent with *in vivo* observations.

Feedback of tree architecture on secondary branch stabilization and orientation

While the dynamics of branches is partly governed by a few constitutive parameters that are homogeneous in space, simulations also revealed the importance of feedback of dendritic tree geomentry on local branch dynamics.

The *in vivo*, observation that a depolymerizing secondary extension (parent branch) does not shrink beyond the branching point of any existing tertiary extensions (child branches) was incorporated in the simulations (Figure S2D, Video6).With this mechanism, child branches protect depolymerizing parent branches from complete shrinkage. When we prevented tertiary and quaternary extensions (child) from forming in simulations, fewer secondary branches (parent) were observed (Figure 4G,H (blue lines)). Thus, tertiary and quaternary extensions reduce the probability of complete branch elimination giving rise to branch self-stabilization.

The most striking feature of secondary branch morphogenesis was self-repulsion, which occurred quite frequently hinting at an important role in patterning. We thus decided to further explore this observation.

When a new extension emerges in a region surrounded by other extensions, its probability of survival strongly decreases, since its probability of encountering neighbors is high. Thus, branching density can feed back negatively on branch number, This in turn affects tertiary extensions as they are more likely to encounter neighbors(Figure S3h (Top)). Our simulations with and without self-repulsion confirmed that self-repulsion strongly reduces secondary branch numbers (Figure 4G-H red and green lines) and lengths (Figure S3H (Bottom)).

Self-repulsion also strikingly impacted dendrite orientation. The distribution of angles made by the secondary dendrites on primary branches both in simulations and experiments peaked at around 90°. Lower frequency values were observed around both 0° and 180°. Thus, secondary dendrites tend to be oriented orthogonally to the primary branch. When contact-induced depolymerization was eliminated we observed a uniform angle distribution (Figure 4I). Hence, in our simulations, the observed orientation of secondary dendrites does not require a guidance cue *per se*, but is an outcome of a branch selection process that minimizes branch density and cross-over through self-repulsion. Thus, self-repulsion is potentially a key feature responsible for the characteristic ‘bottle-brush’ shape of vpda neurons.

Thus, in our model, the dendritic tree geometry which emerges from the local branch dynamics exerts positive (self-stabilization by child-branches) and negative feedbacks (branch elimination and shrinkage through self-repulsion) on branch dynamics by effectively changing the rate of shrinkage.

Dscam1 restricts the orientation of secondary dendrites

To further test our model, we investigated the impact of self-repulsion *in vivo* using *dscam1* mutants. Dscam1 is a type I membrane protein of the immunoglobulin superfamily [55] expressed in all 4 neuronal classes, playing a role in cell identity. Its loss causes self-avoidance defects in all 4 classes of md-neurons[56–58]. All previous studies observed *dscam1* mutants at late stage when dendrite patterning was complete. Thus, how self-avoidance affects the emergence of dendrite patterns remains unknown.

The embryonic development of vpda neurons was observed in $dscam^{P1}$ mutant[55,56] over a *dscam1* deletion line, marked with CD4::neon green. The mutant and control embryos were imaged from 17h to 22hAEL (Figure 5A, Video7). The development of the primary branch was unaffected in the mutant (Figure S4A), with no significant difference in the primary branch length measured at 22hrs AEL (Figure S4B).

At 22h AEL $dscam^{P1}$ dendrites do not appear to share the high branching densities of simulations without self-repulsion (Figure 4G(ii)). We thus carefully examined morphogenesis of *dscam1* mutants to understand how it is different from simulations without repulsion.

Consistent with previous studies performed at later stages, at 22h AEL, mutant dendrites frequently crossed over each other, thereby forming apparent ‘loops’ in the dendrite architecture (Figure 5A (xii),B). These ‘loops’ were also observed to a lesser extent in control dendrites (Figure 5A (vi)). The number of loops increased in both control and mutant embryos from 17 to 19h AEL. However, from 20-22h AEL, the number dropped strongly in controls, but was maintained in mutants (Figure 5C). This meant that from 17h to 19h AEL, the secondary and tertiary extensions explore the space around them and contact their neighbors in both genetic conditions. However, over time these contacts are not maintained in control embryos due to self-repulsion but persist in the *dscam1* mutant.

Additionally, the dendritic field area (Figure 5B measured using the convex hull) covered by the dendrite was smaller in mutants than in controls. The area of the dendrites became significantly smaller in *dscam1* mutants from 19h AEL and was on average 20% smaller at 22h AEL (Figure 5D). The smaller dendritic field areas of $dscam^{P1}$ meant that the secondary branches are either shorter (Figure 5B(Hyp1)) or that they are not perpendicular to the primary branch (Figure 5B (Hyp2)) as seen in simulations without self-repulsion (Figure 4I). To test these hypotheses, we measured secondary branch lengths at 22h AEL and found no significant difference between mutants and controls (Figure 5E). This suggested that the reduced dendritic field is due to a loss of secondary branches that are oriented perpendicular to the primary branch. We measured a significant reduction in the number of perpendicular secondary branches in *dscam1* mutants (Figure 5J). However, the observed angle distribution was flatter than controls but not uniform as predicted by the ‘no-repulsion’ simulations. This suggested that self-repulsion was not completely lost in $dscam^{P1}$ mutants. Upon close inspection, indeed, instances of self-repulsion were observed in the $dscam^{P1}$ movies (Figure 5G, Video8).

We thus modified our ‘no-repulsion’ simulations such that the probability of switching to a depolymerizing state p_{off} was reduced upon contact with neighboring dendrites. Using this modification we tested a range of values for p_{off} while for control simulations $p_{off} = 1$ (Figure 5H). For $p_{off} = 0.1$ (10% probability of retraction after contact) very dense arborization patterns were obtained. Increasing p_{off} resulted in decreased branch densities. Notably, for $p_{off} = 0.5$ the final dendrite morphologies exhibit a tree-architecture similar to control neurons (Figure 5I). Additionally, reducing p_{off} at 16h AEL resulted in highly dense arborization patterns at 22h AEL (for $p_{off} = 0.1$ and $p_{off} = 0.3$). However, when p_{off} was reduced at 18h AEL, the arborization patterns were similar to *in vivo* observations. Hence, we reduced p_{off} at 18h AEL for further analyses.

Next, the angle distribution was measured. We found that for $p_{off} = 0.1$ the distribution was flatter than for $dscam^{P1}$ mutants, while for $p_{off} = 0.3$, it was consistent with $dscam^{P1}$ mutants (Figure 5J). We then measured the number of loops at 22h AEL. For $p_{off} = 0.3$ the number of loops is consistent with $dscam^{P1}$ (Figure 5K) while for $p_{off} = 0.5$ there were significantly fewer loops than *dscam*^{P1}. Thus, our simulations support the experimental observation that self-repulsion is reduced but not fully suppressed in *dscam*^{P1} mutants.

To conclude, self-repulsion patterns secondary branches by restricting direction of secondary extension growth, thus, ensuring a preferential stabilization of secondary branches perpendicular to the primary branch, giving the class I neurons their characteristic shape.

Discussion

Several studies have identified and characterized molecules important for regulating different aspects of dendrite patterning[2,59–63]. However, how a neuron integrates molecular information to generate characteristic dendritic shapes is still unclear. Addressing this type of question requires observing dendrite morphogenesis live and *in vivo*.

Previous descriptions of the embryonic development of the *Drosophila* sensory neurons showed when and how branching was initiated and completed [62,64]. However, to deepen our understanding, precise quantitative descriptions are required. The quantitative description of morphogenesis of the class I vpda neuron in our study showed that the primary dendrite grows deterministically while secondary dendrite morphogenesis is stochastic

Our study shows that the primary dendrite could be guided by an extrinsically patterned cue present at cell-cell interfaces. Cues classically involved in axon guidance like Semaphorins [65,66], Slits [22,24] and Netrins [25] have been implicated in dendrite targeting. Sax-7, extrinsically patterned in *C.elegans* hypodermal cells and guides dendrite patterning of the PVD neuron. It is therefore very likely that such a molecule guides the primary dendrite of the vpda neuron [28]. Interestingly, the cell boundaries along which the primary dendrite grows appear to be stretched as junctions are aligned along the dorsal-ventral axis. MyosinII is enriched along these boundaries [67]. Thus, alternatively cortical tension might guide the primary dorsal branch. Tension could for instance form a path of least resistance through local tissue deformation or provide a stiffer substratum to favor dendrite growth [68]

Secondary dendrite morphogenesis was studied both *in vivo* and *in silico* using a computational model relying on stochastic branching dynamics, with self-repulsion. The onset of secondary branch morphogenesis was very dynamic and as morphogenesis progressed, the dynamics greatly reduced. The computational model demonstrated the necessity to incorporate a decay of kinetic parameters (‘cell aging’) to account for bounded dendrite growth. It is possible that dendrites age through stabilization by microtubules [59,69]. Tagged actin was expressed in the highly dynamic dendritic tips while microtubules were present in the more stable parts of the dendritic tree (data not shown). Thus, aging could require a mechanism that decreases actin dynamics and increases microtubule polymerization over time.

Our model reveals two opposing feedbacks of tree geometry on local branch dynamics. “Child-branches” (tertiary) promote branch survival by having a stabilizing effect on parent branches (secondary). Thus, branches with more children have a higher survival probability. However, a high branching density exerts a negative feedback. Self-repulsion reduces branch survival by introducing a new effective depolymerization rate k'_{off} which is proportional to the product of encounter probability and the probability of switching to a depolymerizing state upon encounter, p_{off}. Remarkably, while all the previously described computational parameters are constitutive quantities of the model, k'_{off} is a variable parameter that depends, among others, on the local branch density. Through this ‘geometric’ feedback, the tree architecture updates its dynamic parameters and affects its own morphogenesis. Thus, self-stabilization and self-repulsion constrain the number and lengths of the secondary branches.

Vpda neuron morphogenesis has also been modeled using optimal wiring constraints and stochastic retraction[70] without explicitly incorporating self-repulsion, yet leading to similar results. This suggests that our simple rules for local dynamics could lead to optimally wired dendrite structures.

Our study revealed another remarkable function of self-repulsion in biasing the orientation of secondary dendrites perpendicular to the primary branch. The prediction from simulations was confirmed *in vivo* through the analysis of the *dscam*^{P1} mutants. During morphogenesis, growing dendrites extend and contact their neighbors. In *dscam*^{P1} mutants, dendrite growth persists in all directions even after self-contact (Figure 5J). Thus, in controls, a given dendrite's final orientation is dependent on where and when it encountered neighbors. Hence, both experimental observations and simulation argue that the dendritic tree-patterns are not guided deterministically, but emerge as self-organized structures through the stochastic interactions during morphogenesis.

The *dscam*^{P1} allele is an intronic P-element insertion, which results in a strong loss of function allele but is not necessarily a null condition. Thus the remnant self-repulsion we observed in *dscam*^{P1} could be the result of an incomplete loss of Dscam1. Alternatively, the remaining self-repulsion could also reflect the activity of multi-pass trans-membrane proteins Flamingo[71] and Wntless[72] and immunoglobulin superfamily proteins like Turtle[73] have all been shown to play a role in self-repulsion.

The *dscam*^{P1} dendrites were not longer than controls as predicted by the no-repulsion simulations (Figure 5E). However, *dscam*^{P1} significantly increases the length of the non-orthogonally aligned dendrites (Figure S4C). Also, unlike the model prediction, the number of secondary branches in the *dscam*^{P1} mutants was significantly lower than in control dendrites (Figure S4D) suggesting a role in branch stabilization. Thus, self-repulsion may not account for all the function of Dscam1. Dscam1 is a complex molecule that could have several unknown functions. One possibility is that its loss might impinge on a signaling pathway necessary for stabilization of secondary extensions.

While our data reveal new insights on the self-organizing properties of dendrites, our observations do not rule out the possibility that extrinsically patterned cues are also involved in secondary branch morphogenesis of vpda neurons. For example, the anterior-posterior asymmetry in secondary branch length of the vpda neuron (data not shown) depends on extrinsically patterned Ten-m [74]. We suggest that self-organizing principles reported in this study could provide a 'ground state' upon which additional cues could operate in other neuronal classes. The role of extrinsic cues would have to be analyzed in the background of stochastic branching processes and geometric feedbacks, which, by themselves provide a spatial bias to dendrite growth. However, extrinsic cues can also profoundly control patterning as described in *C.elegans* PVD neurons[28,38–40]. Thus, the type of cue (extrinsic or intrinsic) that plays major instructive roles is context dependent.

This study highlights the dynamics of dendrite growth and provides the analytical basis for further investigating dendrite dynamics and patterning *in vivo*. It will be particularly interesting to explore, based on this study, how class specific morphology of multi-dendritic neurons emerges, as a function of varying class-specific self-organizing rules of arborization. We suggest that such intrinsic rules, though statistical, might be genetically encoded. Ultimately, understanding how genes determine statistical rules of branching provides an opportunity to understand how, in a broader context, genes encode form.

AUTHOR CONTRIBUTIONS

A.P. and T.L. conceived the project and planned experiments. A.P. performed all experiments, quantifications and data analysis. N.T.-E. and J.-F.R. designed the model and the computational simulations; N.T.-E. obtained the numerical results. All authors analyzed the results and wrote the manuscript.

ACKNOWLEDGEMENTS

We thank all members of the Lecuit lab for very useful discussions throughout the course of this work, for creating a stimulating environment, and also for critical comments on the manuscript. We thank members of A.P.'s thesis jury, Markus Affolter, Edouard Hannezo and Peter Soba for fruitful and insightful comments. We thank Jean-Marc Philippe for generating the neon green fly line and Benoit Aigouy for the 'Dendrite arborization Tracer'. We are grateful to the IBDM imaging facility for assistance with maintenance of the Microscopes, and FlyBase for maintaining curated database and Bloomington fly facility for providing transgenenic flies. A.P. was supported by Ph.D. fellowship from the LabEx INFORM (ANR-11- LABX-0054) and of the A*MIDEX project (ANR-11-IDEX-0001-02), funded by the "Investissements d'Avenir French Government program". NT-E was supported by the "Investissements d'Avenir French Government program" managed by the French National Research Agency (ANR-16-CONV-0001) and from the Excellence Initiative of Aix-Marseille Univerité - A*MIDEX. We acknowledge France-BioImaging infra- structure supported by the French National Research Agency (ANR-10-INBS-04-01, «Investments for the future»).

TABLES

Table 1. Computational parameters

Parameters		Notation	Option 1	Option 2
Time step ($\mathbf{min}$)		Δt	0.5	0.5
Length primary branch ($\mu\mathbf{m}$)		L_1	30	30
Number of beads in primary branch		N_1	100	100
Branching rate ($\mu\mathbf{m}^{-1}\ \mathbf{min}^{-1}$)	Secondary	λ_1	0.22	0.12
	Tertiary	λ_2	0.05	0.05
	Quaternary	λ_3	0.02	0.02
Growth/shrink rates ($\mu\mathbf{m}\ \mathbf{min}^{-1}$)	Secondary	$v_{2,on/off}$	0.62	0.32
	Tertiary	$v_{3,on/off}$	0.31	0.18
	Quaternary	$v_{4,on/off}$	0.31	0.18
Persistence length ($\mu\mathbf{m}$)		l_p	17	17
Spontaneous switching rate to a polymerizing state ($\mathbf{min}^{-1}$)		k_{on}	0.5	0.67
Spontaneous switching rate to a depolymerizing state ($\mathbf{min}^{-1}$)		k_{off}	0.67	0.67

STAR METHODS

KEY RESOURCES TABLE

REAGENT or RESOURCE	SOURCE	IDENTIFIER
Antibodies		
Rabbit polyclonal anti-GFP	Thermo Fisher Scientific	Cat # PA1-980A, RRID:AB_325960
Goat anti-Rabbit Alexa Fluor® 488	Thermo Fisher Scientific	Cat # A32731 RRID:AB_2633280
Chemicals, Peptides, and Recombinant Proteins		
Ryanodine	Merck	Cat# 559276-500UG
Experimental Models: Organisms/Strains		
D. melanogaster . 2-21 gal4	Parrish *et al.*, 2006 [75]	Flybase ID: FBal0328157
D. melanogaster. Mhc^1	O'Donnell and Bernstein 1988 [76]	Flybase ID: FBal0012242

D.melanogaster. UAS-CD8::GFP y[1] w[*]; P{w[+mC]=UAS-mCD8::GFP.L}LL5, P{UAS-mCD8::GFP.L}2	Bloomington Drosophila Stock Center	BDSC:5137 Flybase ID: FBti0012685
D. melanogaster: Ecad::Tomato y[1] w[*]; TI{TI}shg[mTomato]	Bloomington Drosophila Stock Center	BDSC: 58789 Flybase ID: FBti0168570
D. melanogaster. $dscam^{P1}$ P{ry[+t7.2]=PZ}Dscam1[05518] cn[1]/CyO; ry[506]	Bloomington Drosophila Stock Center	BDSC: 11412 Flybase ID: FBti0002607
D. melanogaster: ΔDscam1 w[1118]; Df(2R)ED1673, P{w[+mW.Scer\FRT.hs3]=3'.RS5+3.3'}ED1673/SM6a	Bloomington Drosophila Stock Center	BDSC: 9062 Flybase ID:
D. melanogaster. UAS-CD4::neongreen	This paper	N/A
Recombinant DNA		
pACU2_CD4-mIFP T2A HO1	Yu *et al.*, 2015 [77]	RRID:Addgene_72441
Software and Algorithms		
MATLAB R2018a	MathWorks	RRID:SCR_001622
Fiji	Schindelin et al., 2012 [78]	RRID:SCR_002285 https://fiji.sc
Dendrite Arborization Tracer	This paper	N/A

RESOURCE AVAILABILITY

Lead Contact

Further information and requests for resources and reagents should be directed to and will be fulfilled by the Lead Contact, Thomas Lecuit (thomas.lecuit@univ-amu.fr).

Materials Availability

This study did not generate new unique reagents.

Data and Code Availability

The codes generated during this study are available upon request.

EXPERIMANTAL MODEL AND SUBJECT DETAILS

The experiments were performed *on Drosophila melanogaster* embryos and larvae. The adult flies maintained under the standard lab conditions in plastic vials at 18°C or 25°C with yeast food. Embryo collection was done in cages with agar plate made with apple juice, supplemented with yeast paste. Flies lay eggs on these plates and embryos are filtered from the yeast paste by distilled water. Larvae were grown in plastic vials at 25°C and collected at 24h, 48h, 72h and 96h AEL.

METHOD DETAILS

Embryo imaging assay

The muscular tissue is established at the stage of observation; hence, muscle contraction prevented the capture of stable and time resolved images. A previous study suggested dendritic development was normal in mutants for muscle myosin, which paralyzes embryos[79]. Therefore, vpda neurons labeled with CD8::GFP (with the 2-21Gal-4 line) were imaged in a myosin heavy chain mutant background [76] to prevent muscular contractions. No statistically significant difference in neuron morphology was observed in mhc1 mutant embryos (Figure S1E-H), suggesting that mhc1 mutants provide an effective solution to temporally resolve embryonic dendrite morphologies.

When, recombining the mhc[1] mutant allele with the *dscam*^{P1} mutant proved to be difficult; in these experiments, Ryanodine (a drug that inhibits muscle contractions by binding to the ryanodine receptor and preventing calcium release into the sarcoplasmic reticulum) was injected into stage 16 embryos. Single images of water and ryanodine injected vpda neurons were captured 10 hours after injection. Analysis revealed no major defects in dendrite morphology, apart from small but significant increase in the number of secondary branches in the ryanodine injected embryos (Figure S1I-L). As there were no other patterning differences, the ryanodine-injected embryos still offered an effective solution to obtain time resolved images of *dscam*^{P1} mutant embryos. In Ryanodine injected embryos, muscle contractions are reduced but not completely gone, thus, the out of focus images are deleted from the movies.

Embryo preparation for live imaging

Embryos were prepared as described before[80]. In brief, embryos were de-chorionated using bleach, for about 1 minute and then washed thoroughly with distilled water. The embryos were then aligned ventro-laterally on a flat piece of agar and then glued to a glass coverslip. These embryos can be submerged in halocarbon oil and can be imaged directly. Alternatively, glued embryos (;*dscam*^{P1}/ΔDscam1;2-21gal4, UAS-CD4::neongreen/''; 2-21gal4 and ;;UAS-CD8::GFP/''; 2-21gal4) were kept in an airtight box containing Drierite for about 7 min, then covered in halocarbon oil, and then injected with Ryanodine. Ryanodine was injected at a concentration of 50mM in mid stage 16 embryos about 10 minutes prior to imaging using a FemtoJet 4i microinjector by Eppendorf and then imaged at the microscope.

Larval preparation for live imaging

For analysis of dendrite morphology at different stages of development, whole larvae at L1, L2 and L3 were placed in a watch glass with a few mL of 1mM Sodium Azide to paralyze them and then mounted in low melting agarose to be imaged on a lightsheet microscope so that the larvae could be rotated and all the neurons could be easily imaged.

Immunostaining

Homozygous 2-21gal4/UAS-mCD8::GFP larvae (96h±3) were filleted using standard protocols[81] Briefly, the larvae were washed with PBS and pinned on PDMS plates, keeping the dorsal side upright, with dissection pins between the mouth hooks and posterior spiracles. Fine dissecting scissors were used to open the larvae along the center from posterior to anterior. Forceps were used to carefully remove the gut. The anterior and posterior ends were then pinned laterally to obtain the fillet and fixed in 4%PFA for 15min and stained with a rabbit anti-GFP antibody (1:500,). Secondary antibodies conjugates with Alexa488, were used 1:500. The stained larvae were mounted in VECTASHIELD®.

Image Acquisition

For live imaging embryos were prepared as described earlier and time-lapse imaging was performed with a dual camera spinning disc (CSU-X1, Yokogawa) Nikon Eclipse Ti inverted microscope (distributed by Roper) using a 100X/N.A 1.4 oil-immersion objective. The system acquires images using the Meta-Morph software and images were taken as z-series of 1.5μm

X10 planes spanning 13.5μm and acquired with a frame rate of 3min for 10hours or 30min for 10 hours or 30s for 1hour.

For whole mount imaging, larvae were treated as described before and imaged on a Zeiss Lightsheet Z.1 on a 20X/N.A 0.8. The system acquires images using ZEN software conditions were kept consistent for all 3 stages.

Fixed larval fillets were imaged on a Zeiss LSM 880 on a 25X/N.A 0.8. The system acquires images using the ZEN software and image stacks with spacing of 0.15–0.2 μm were collected and stack focused projections of 7-10 planes analyzed.

Laser Ablations

Ablations were performed at around 15-16h AEL on an inverted microscope (Eclipse TE 2000-E; Nikon) equipped with a spinning-disc (Ultraview ERS, Perkin Elmer) for fast imaging. Time lapse at a single z-plane was acquired using a ×100 1.4 NA oil immersion objective. Ablations were performed in parallel with image acquisition. Ablation events were obtained by exposing the primary dendrite, for duration of 2–3 ms, to a near-infrared laser (1030 nm) focused in a diffraction-limited spot. Laser power at the back aperture of the objective was ~400mW. Once ablated, the neurons were imaged on the dual camera, spinning disc (CSU-X1, Yokogawa) Nikon Eclipse Ti inverted microscope (distributed by Roper) using a 100X/N.A 1.4 oil-immersion objective as described above. In these experiments, the control neurons were the unablated neurons from the neighboring segments.

Image Processing and Segmentation

CD8::GFP or CD4::neongreen was used to label the neuronal cell membranes. A custom ImageJ macro integrating the Stack Focuser plugin from M. Umorin was used to project (by maximum intensity projection the z-planes with signal from the neuron. This resulted in sharper cell outlines and better S/N ratio compared with maximal projections. The 2D projected stacks were then segmented using a custom 'Dendritic Arborization Tracer' from B. Aigouy.

Computational model

We developed a two-dimensional stochastic branching model with contact-induced branch depolymerization (or self-repulsion). In contrast to other branching models for morphogenesis [34], we include the possibility of branch retraction.

In our simulations, the dendrite structure is discretized into elementary spatial units (hereafter referred to as beads). At the simulation time $t = 0$ (approximately corresponding to the developmental time $t = 15$h AEL), we consider a pre-existing primary branch composed by a constant number of beads $N_1 = 100$ (corresponding to $L_1 = 30$μm) and situated along the y-axis.

<u>Branching</u>. At each time step Δt, a new secondary branch is created from a non-branched bead with a probability denoted by

$$P_{b,2} = \lambda_1 \Delta l_1 \Delta t,$$

where Δl_1 is the inter-bead spacing in the primary branch; λ_1 is the branching rate of secondary branches. After 1h of evolution (corresponding to t = 16h AEL), tertiary and quaternary branches are created using the same mechanism. Similarly, we define the per-bead new tertiary (resp. quaternary) branch creation probability $P_{b,3} = \lambda_2 \Delta l_2 \Delta t$ from a secondary bead (resp. $P_{b,4} = \lambda_3 \Delta l_3 \Delta t$ from a tertiary bead), where $\Delta l_{2/3}$ is the bead interspacing for secondary (resp. tertiary) branches and $\lambda_{2/3}$ is the branching rate of tertiary (resp. quaternary) branches. Whenever a new branch (called a child branch) is created, we place the first bead of the newly created child branch at the coordinate location:

$$x_{i,child} = x_{parent} + \Delta l_i \cos\theta$$
$$y_{i,child} = y_{parent} + \Delta l_i \sin\theta$$

where (x_{parent}, y_{parent}) is the coordinate of the parent bead, the index i runs for the order of complexity of the branch and θ is chosen according to a uniform distribution on $[0,2\pi]$.

Polymerization/depolymerization. We assume that branches are either in a polymerizing or a depolymerizing state. A branch in a polymerizing state grows with a rate $v_{i,on}$, where the index i again runs for the order of complexity of the extension. In this way, at each time step Δt the number of beads of the branch is incremented by one. The position of the new bead j is:

$$x_{i,j} = x_{i,j-1} + \Delta l_i \cos \varphi_{i,j}$$
$$y_{i,j} = y_{i,j-1} + \Delta l_i \sin \varphi_{i.j}$$
$$\varphi_{i,j} = \varphi_{i,j-1} + \sqrt{\frac{2\Delta l_i}{l_p}}\eta$$

where $(x_{i,j-1}, y_{i,j-1})$ is the position of the previous bead in the branch, η is a centered unit Gaussian variable and l_p is the persistence length of the dendrite branch. We considered a persistence length of $l_p = 17\mu\text{m}$, which is consistent with values measured in the actin bundles [82] (see Table 1).

Conversely, a branch in a depolymerizing state shrinks with a rate $v_{i,off}$. Experimental branch tracking suggest that we can set $v_{i,on} = v_{i,off}$. Depolymerization then occurs through removal of beads at the branch tip. We prevent branch depolymerization beyond a forking bead. If a child was created from this bead, the parent branch changes to a polymerizing state and starts to grow again. A branch disappears if its last bead is removed through depolymerization.

Spontaneous switching. We define the rates k_{on} (resp. k_{off}) for branches to switch from a depolymerizing (resp. polymerizing) state to a polymerizing (resp. depolymerizing) one. In our simulation, at each time step Δt we evaluate whether a branch should switch from a depolymerizing state to a polymerizing state; the switch occurs stochastically every time we find that a random variable uniformly distributed on (0,1), denoted U, satisfies the relation:

$$U < 1 - e^{-k_{on}\Delta t}.$$

Therefore, the mean duration of polymerization phases read $\tau_{on} = 1/k_{on}$. Similarly, the statistics of the switch from polymerization to depolymerization is evaluated according to a rate denoted by k_{off} (and τ_{off}).

Contact-induced depolymerization. Whenever the distance between the last new bead of a polymerizing branch and any bead of other branches is smaller than a certain threshold d_{th}, depolymerization is implemented with probability p_{off}. The case p_{off}= 1 corresponds to the control case; we find that p_{off} = 0.3 provides a satisfactory fit of the *dscam^{p1}* mutant case.

Aging. We implemented a progressive reduction in the values of the dynamic parameters at regular time intervals (corresponding to 2h experimentally). In particular, both the branching and switching rates, λ_i and $k_{i,on/off}$ respectively, are reduced by a factor f_i, with i being the order of complexity of the branch, while the polymerizing and depolymerizing rates, $v_{i,on/off}$, are reduced by a different factor $f_{v,i}$. At each reduction, we re-mesh each branch with a new interspacing given by $v_{i,on}f_{v,i}\Delta t$ (with $v_{i,on}$ the initial growth rate), which amounts to increasing the number of beads. The interplay between the possible values of f_i and $f_{v,i}$ defines the two aging protocols presented in the main text (see also Figure 4D).

QUANTIFICATION AND STATISTICAL ANALYSIS

Data Analysis

The 'Dendritic Arborization Tracer' provides skeletonized images in such a way every segment (connected to other segments through vertices) is assigned a unique identity (Figure S1B). We then ordered these individual segments using MATLAB (including Curve Fitting Toolbox, Image Processing Toolbox, Statistics and Machine Learning Toolbox). Starting from the cell body we connected segments that made the longest line and assigned it to be the primary branch. Similarly, we then connected all the segments making the longest lines starting from the primary branch to be secondary branches and so on (Fig. S1c). However, our code does account for loops in the dendritic tree. In the wild-type, the dendrites rarely crossed each other, however, in the event of a crossing, we manually removed the loops (only when we looked at normal growth (Figure1)). We then performed all our analysis on this processed skeleton of the dendrite. To plot data, we used Matlab (the IoSR box Plot function by Christopher Hummersone).

When we compared control and *dscam1* mutants, loops in the dendritic tree prevented us from using the software, thus, the movies of development in both conditions were segmented using the 'Dendritic Arborization Tracer' but the dendrites were ordered manually by observing the movies of embryonic development.

Statistics

For all experiments data points from different neurons/embryos from at least 3 independent experiments were pooled. For each box, in the box plots, the central line is the median, the 'o' is the mean, the box extends vertically between the 25th and 75th percentiles, the whiskers extend to the most extreme data that are not considered outliers, and the outliers are plotted individually. All the P values are calculated using a two-sided non-parametric Mann–Whitney test (Matlab statistics toolbox) except in Figure 5J where P values are calculated using the two sample Kolmogorov-Smirnov test. The exact values of n and what it represents for each graph are reported in the figure legends. The experiments were not randomized and the investigators were not blinded to allocation during experiments and outcome assessment.

FIGURES

Figures

Figure 1. Dendrite patterning is nearly complete by the end of embryogenesis
(a) Images of Class I vpda neurons taken from homozygous 2-21gal4/UAS-mCD8::GFP embryos and larvae at the following stages: late embryo (E17 19h AEL±2), 1st instar (L1 24h AEL±3), 2nd instar (L2 48h AEL±3), 3rd instar (L3 72h AEL±3) Schematic: Primary branch (blue) Secondary branches (cyan) Tertiary (brown) Quaternary (red). (b) Quantification of the number of branches at each order of complexity in the neuron. E17 n=26, L1 n=48, L2 n=50 L3 n=38 neurons. (c) Relative distance (Inter dendrite distance/primary branch length) across the 4 stages. E17 n=194, L1 n=374, L2 n=409 L3 n=341 inter-dendrite segments (d) Top panel: Time-lapse images of dendrite development of 2-21gal4/UAS-mCD8::GFP mhc1 mutant background embryos from ~15h AEL to ~25h AEL (Movie1). Lower panel: Schematic representation of dendrite development. Indigo represents stable dendrites and orange represents dynamic extensions. (e) Number of Secondary Branches from 17-25h AEL. (f) Lengths of Secondary Branches from ~17-25h. (g) Number of Tertiary Branches from 17-25h AEL. (h) Length of Tertiary Branches from ~17-25h AEL for (e)-(h) AEL n=16 neurons. For each box, the central line is the median, the 'o' is the mean, the box extends vertically between the 25th and 75th percentiles, the whiskers extend to the most extreme data that are not considered outliers, and the outliers are plotted individually. Statistical significance has been calculated using Mann-Whitney U test for (b) and (c) Not significant= ns, * $p<0.05$; ** $p<0.01$, *** $p<0.001$. All the panels have the same orientation: dorsal at the top, anterior to the left. Scale bars = 10μm.

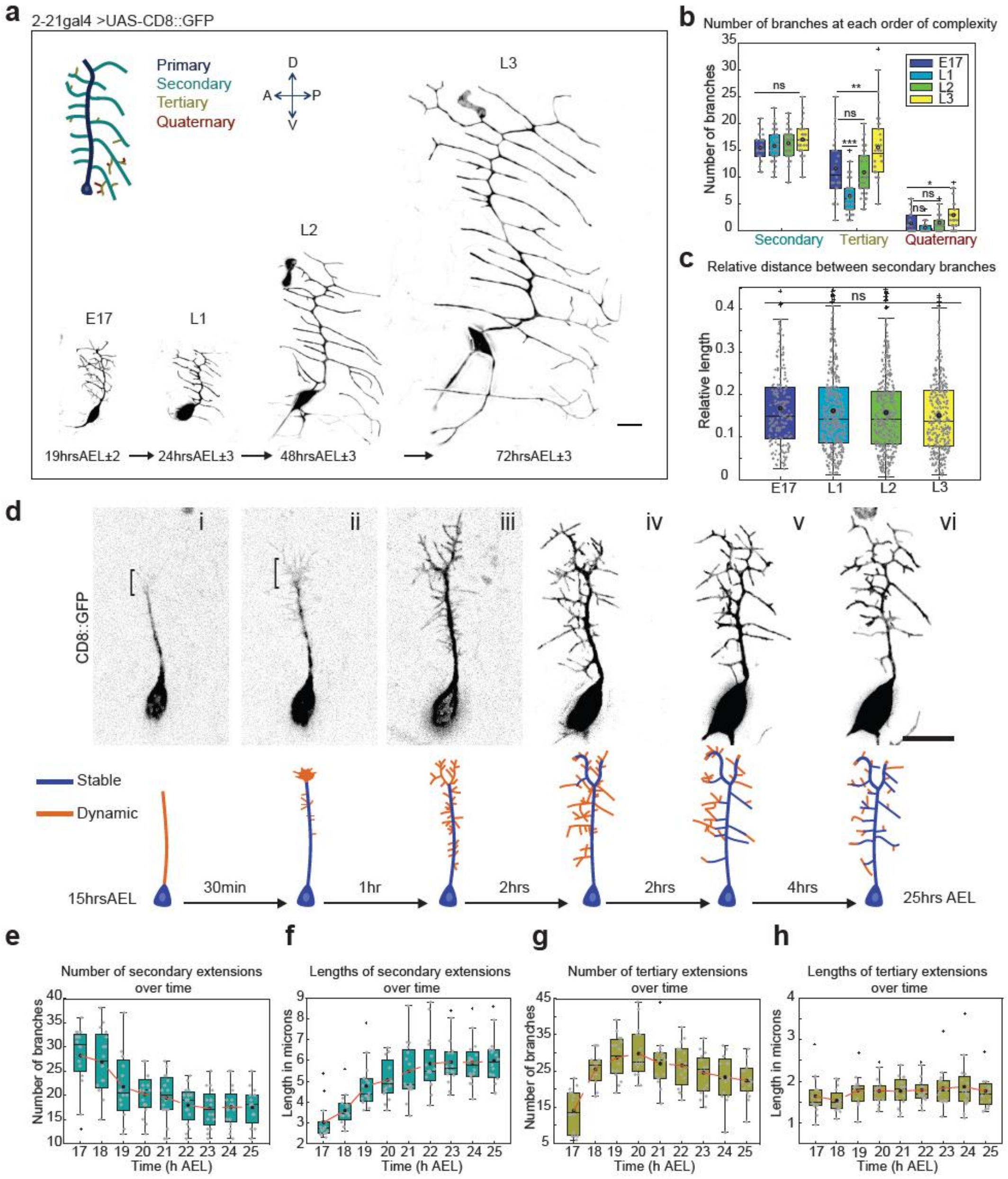

Figure 2. Development of the primary branch is consistent with deterministic growth
(a) Time-lapse images of the uni-directional growth of the primary dendrite during development of 2-21gal4/UAS-mCD8::GFP, mhc1 embryos from ~14h to 15h AEL (Movie2). (b) Image of neuron at ~15h AEL co-imaged with Ecad::tomato. Inset: Close up of primary dendrite following Ecadherin cell boundaries as indicated by the white arrowheads. (c) Schematic: Control and ablated neurons part of the same embryo. Red cross indicates site of ablation. Top Panel: Dendrite development of Control neuron (Movie3). Bottom panel: Dendrite development of ablated neuron (Movie4). Dashed line indicates point of ablation throughout development. Scale bars = 10μm.

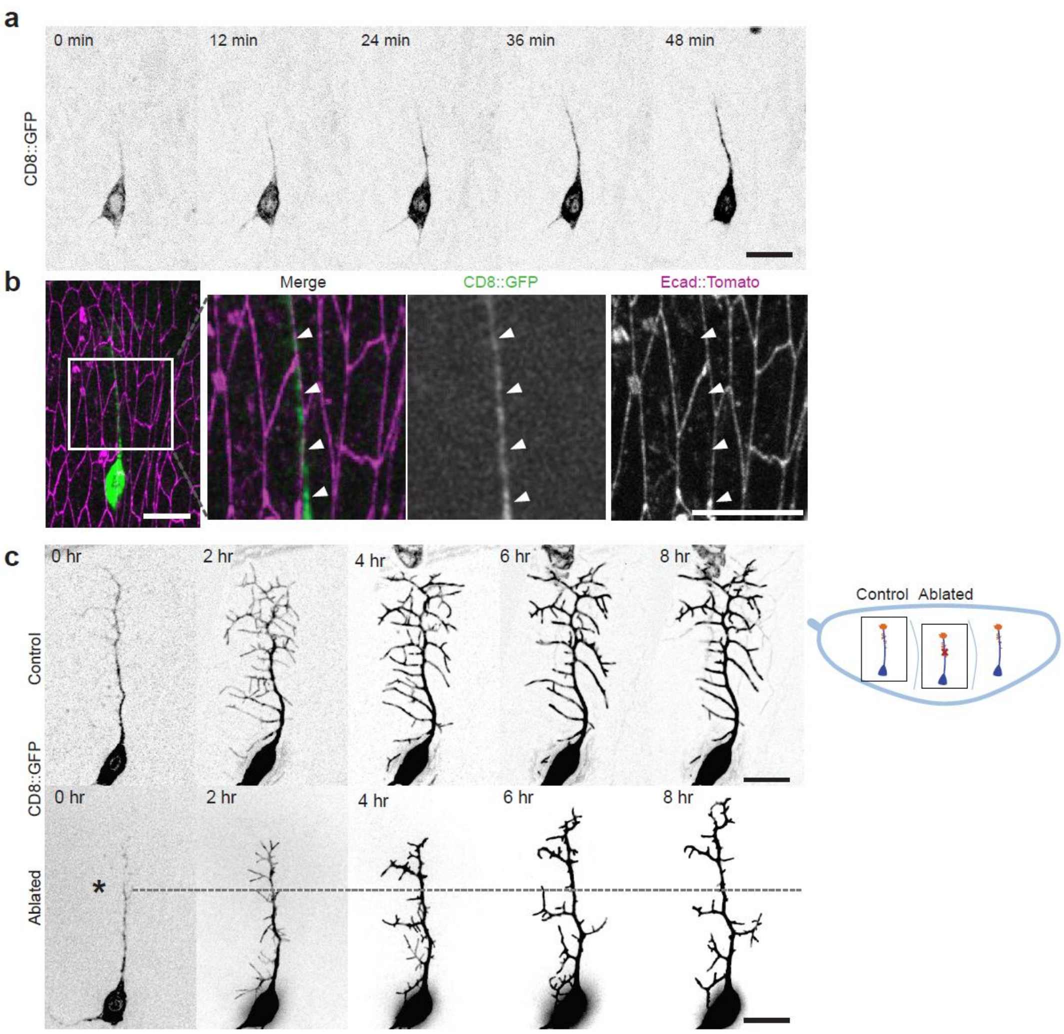

Figure 3. The development of the secondary dendrites is consistent with stochastic growth
(a) Schematic: Larval filet (indicating vpda neurons in the abdominal hemi segments. Neurons in segment A3 were used for analysis. Images of A3 Left and Right vpda neurons at 96h AEL ±3 from homozygous 2-21gal4/UAS-mCD8::GFP larvae. The panel has the following orientation: Anterior at the top, Posterior at the bottom, ventral is the center and dorsal to the sides. (b) Distribution of the total number of Secondary Branches n=42 (21 left-right pairs). (c) Distribution of difference in number of Secondary branches between the left-right pairs. (d) Distribution of primary branch lengths n=66 dendrites from 66 neurons (e) Distribution of Secondary branch lengths analyzed from homozygous 2-21gal4/UAS-mCD8::GFP embryos at 22h AEL ±2 n=1140 branches from 66 neurons (f) Neuron at ~18hAEL.Time-lapse of secondary branch development (Movie5). (i) Green arrowheads indicate extension of a single secondary extension and magenta arrowheads indicated retraction of the same secondary extension. (ii) Blue arrowheads indicate examples of self-repulsion. Panel orientation: dorsal at the top, anterior to the left. (g-i) Lengths of secondary extensions over time, at 17h (g) 20h (h) and 24h AEL (i). The two trend lines indicate two individual branches at each time point. (j) Velocities of secondary extensions at 17, 20 and 24hAEL. Scale bars = 10μm.

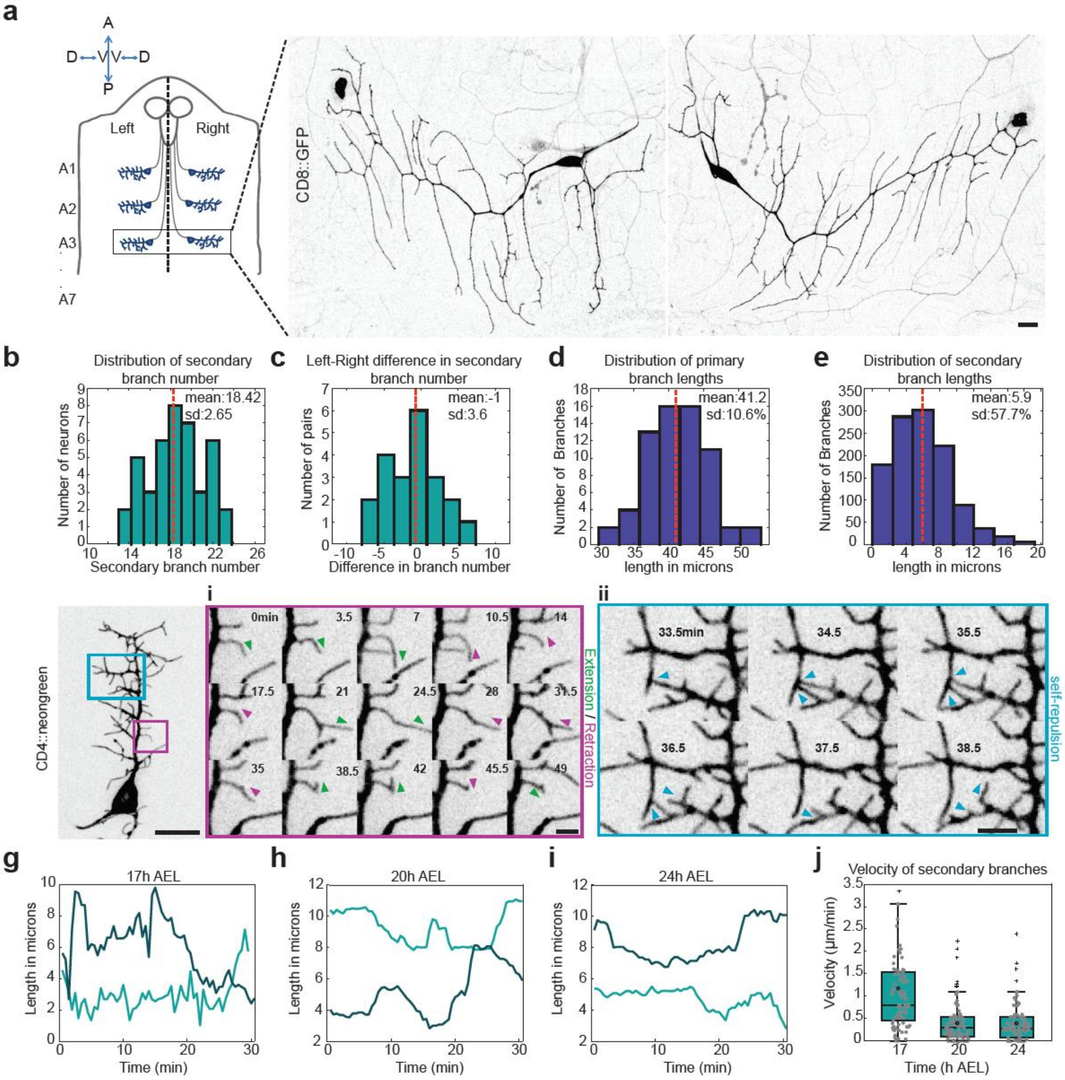

Figure 4. A computational model of dendritic branching and feedback of tree architecture on secondary branch stabilization and orientation

(a) Schematic representation of the mechanisms described in the computational model. (b) Snapshot of a dendritic architecture at 25h AEL from one simulation. (c) Diagram of dendritic morphologies at 25h AEL for different values of the ratio of spontaneous switching rates $r = k_{on}/k_{off}$ and growth rate of secondary branches $v_{2,on}$. The growth rates of tertiary and quaternary branches are given by $v_{3/4,on} = v_{2,on}/2$ and the values of the other computational parameters are fixed and detailed in Table 1, Option 1. (d) Scheme of the aging protocols AP1 and AP2 implemented for $r = 0.75$ and $r = 1$, respectively. The reduction were performed every 2h and the scheme shows the resulting percentage of the initial parameter value after the reduction at each interval. The depolymerization and switching rates $v_{i,off}$ and $k_{i,off}$ are reduced using the same protocol that for $v_{i,on}$ and $k_{i,on}$, respectively. (e) Number of secondary branches and (f) Number of tertiary branches over time from 16-25h AEL. Both in (e) and (f), blue lines represent simulations without aging implementation, red lines represent simulations with the two different aging protocols and the boxes represent the experimental data. (g) Snapshots of the dendritic structures at 22h AEL for three different situations: with self-repulsion and child branches, existence of child branches but suppression of self-avoidance and with self-repulsion but without child extensions. (h) Main: Number of secondary branches over time from 16-22h AEL for the models with self-repulsion and child branches (red line) and with child extensions but no self-avoidance (green line) using AP1. Inset: Number of secondary branches over time from 16-23h AEL for the models with self-repulsion and child branches (red line) and with self-avoidance but no child extensions (blue line) using AP1. (i) Probability distribution of the angles between primary and secondary branches, measuring at the end point, at 22h AEL. The histograms represent *in vivo* observations while red and green lines represent simulations with and without self-repulsion interactions using AP1. Similar results than the one showed in (h) and (i) for AP2 can be found in Fig. S4i-j. The number of simulations for blue lines in (e) and (f) was $N_{sim} = 50$ and for red lines in (e) and (f), and all cases in (h) and (i) was $N_{sim} = 500$. In all figures, simulation lines represent the average value of the realizations and shadows represent the 1σ confidence interval. In addition, a 2-point time-averaging was performed using spline interpolation for lines in (e), (f) and (h). For $r = 0.75$ and AP1 in (e) and (f), and all cases in (g), (h) and (i) the initial values of the computational parameters are detailed in Table 1, Option 1. For $r = 1$ and AP2 in (e) and (f) the initial values of the computational parameters are detailed in Table 1, Option 2. For each box corresponding to *in vivo* observations, the central line is the median, the box extends vertically between the 25th and 75th percentiles and the whiskers extend to the most extreme data that are not considered outliers.

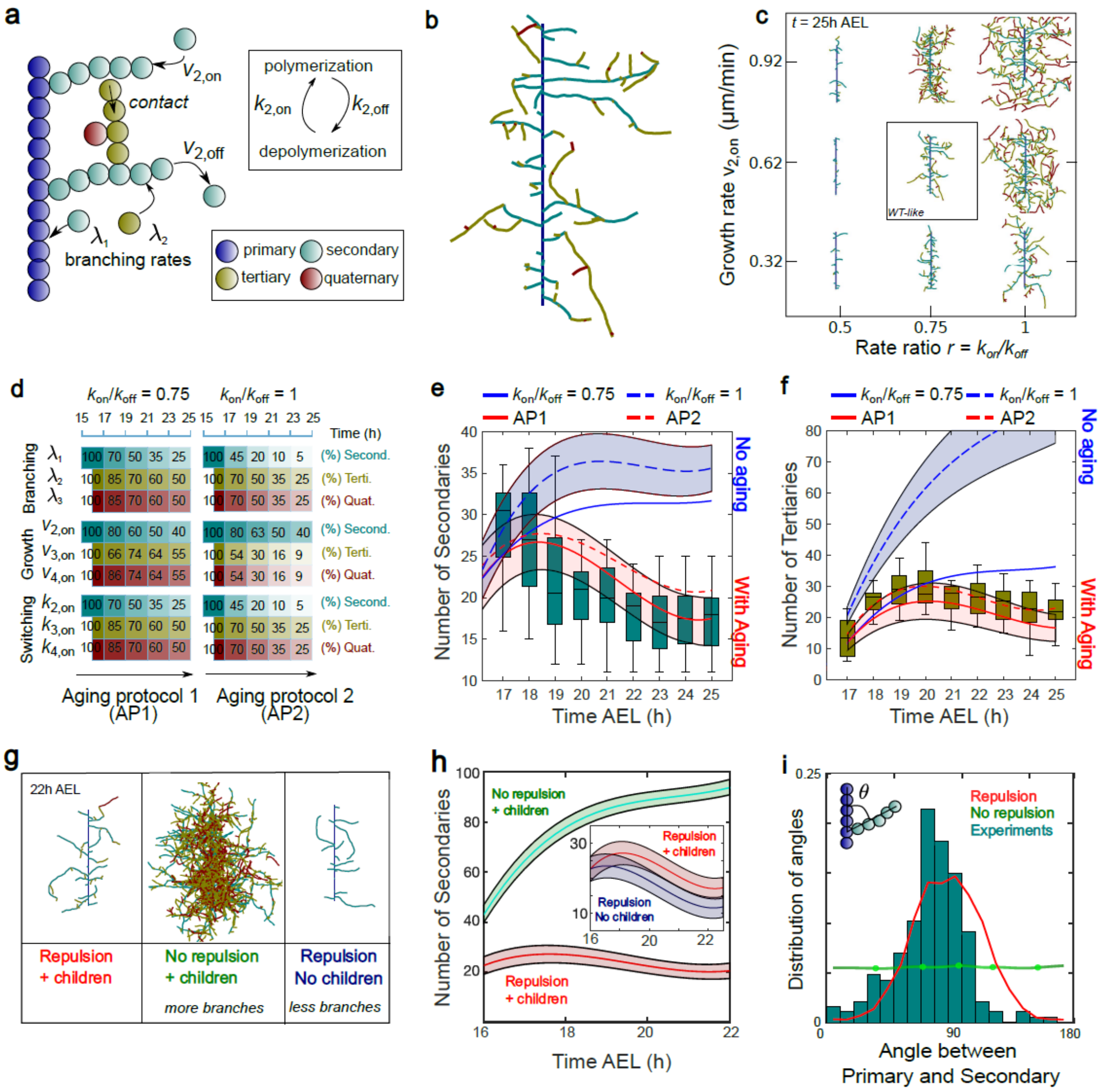

		$k_{on}/k_{off} = 0.75$					$k_{on}/k_{off} = 1$					
Branching	λ_1	100	70	50	35	25	100	45	20	10	5	(%) Second.
	λ_2	100	85	70	60	50	100	70	50	35	25	(%) Terti.
	λ_3	100	85	70	60	50	100	70	50	35	25	(%) Quat.
Growth	$V_{2,on}$	100	80	60	50	40	100	80	63	50	40	(%) Second.
	$V_{3,on}$	100	66	74	64	55	100	54	30	16	9	(%) Terti.
	$V_{4,on}$	100	86	74	64	55	100	54	30	16	9	(%) Quat.
Switching	$k_{2,on}$	100	70	50	35	25	100	45	20	10	5	(%) Second.
	$k_{3,on}$	100	85	70	60	50	100	70	50	35	25	(%) Terti.
	$k_{4,on}$	100	85	70	60	50	100	70	50	35	25	(%) Quat.

Figure 5. Dscam1 dependent self-repulsion restricts orientation of dendrite development
(a) Top panel: Time-lapse images of dendrite development of 2-21gal4/UAS-mCD4::neongreen (Movie8) Lower panel: Time-lapse images of dendrite development of *dscam*^{P1}/ΔDscam1; 2-21gal4/UAS-mCD4::neongreen (Movie9). The embryos were injected

with Ryanodine. Imaged from ~17h AEL to ~22h AEL.(b) Schematic: Area is calculated as the area of the convex hull that contains the dendrites. Red shaded area indicates the loops formed by dendrite crossovers. Top panel: Control dendrites Bottom panel: *dscam*^{P1} dendrites could have a smaller area because of shorter dendrites (ii) or dendrites that are not perpendicular.(c) Number of loops in the dendritic tree ~17-22h AEL. (d) Area of the dendritic field covered by the dendrites ~17-22h AEL. .(e) Quantification of mean secondary branch lengths ~17-22h AEL. For (c) and (d) and (e) Control (blue) n=9 Mutant (green) n=11 (f)Loss of repulsion: Red arrows indicate a dendrite crosses over another branch and does not retract. (g) Remnant repulsion: Red arrows indicate an example of remnant self-repulsion *dscam*^{P1} (Movie10). (h) Schematic: Upon contact with a neighbor, an extension either crosses over its neighbor with a probability of $1 - p_{off}$ or switches to a depolymerizing state with a probability p_{off}. (i) Diagram of dendritic morphologies obtained in simulations at 22h AEL for different values of p_{off} introduced at different developmental time points. (j) Number of loops at 22h AEL for Control experiments, simulations with self-repulsion ($p_{off} = 1$), *dscam*^{P1} , $p_{off} = 0.3$, $p_{off} = 0.5$. The number of simulations for all cases was $N_{sim} = 50$. (k) Probability distribution of angles between primary and secondary branches Control(blue histogram) n=187, Mutant(green histogram), n=124 ks test $p = 0.0113$. Simulation control (red), $p_{off} = 0.3$ (orange), $p_{off} = 0.1$ (yellow). Simulation lines represent the average over $N_{sim} = 100$. For each box, the central line is the median, the 'o' is the mean, the box extends vertically between the 25th and 75th percentiles, the whiskers extend to the most extreme data that are not considered outliers, and the outliers are plotted individually. Statistical significance for (c), (d) & (e) has been calculated using Mann-Whitney U test. ns, * p<0.05; ** p<0.01, *** p<0.001. All the panels have the same orientation: dorsal at the top, anterior to the left. Scale bars = 10µm. In all the simulations, the implemented aging protocol is AP1 (Fig. 4d) and the initial values of the computational parameters are detailed in Table 1, Option 1.

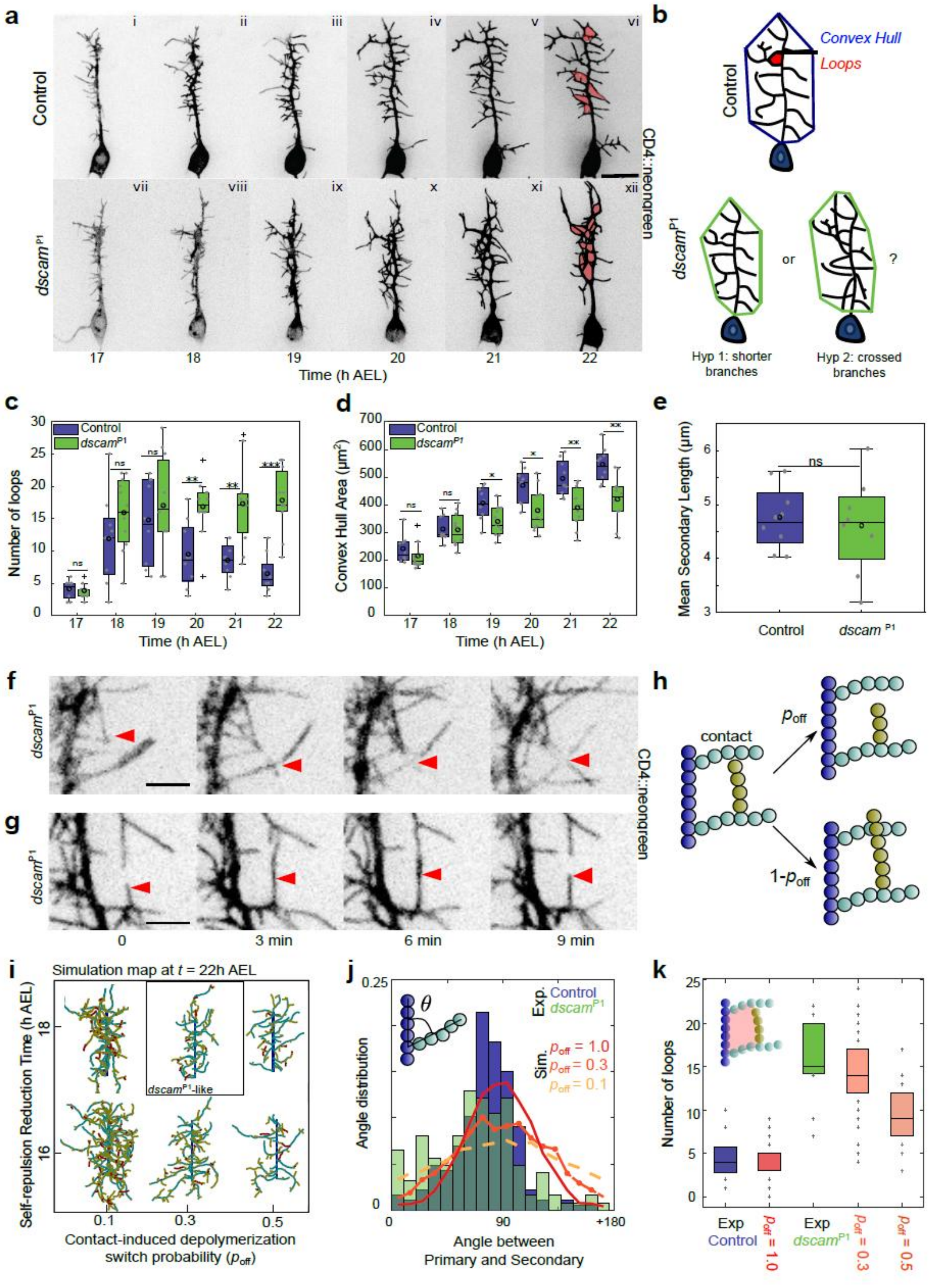

Supplementary Figures

Figure S1. Branch ordering class I vpda neuron and blocking muscular contractions

(a) Class I vpda neuron at the 3rd instar (L3 72h AEL±3) (b) Skeletonized neuron obtained from 'Dendritic Arborization Tracer'. Every segment (length of dendrite between two vertices) has a unique identity represented by different colours. (c) Processed dendrite classified into 4 orders of complexity. Primary (Indigo), Secondary (blue), Tertiary (green), Quaternary (yellow). (d) Quantification of the percentage composition of total dendrite length. E17 n=26, L1 n=48, L2 n=50 L3 n=38 neurons (e) Control Class I vpda neurons taken from homozygous 2-21gal4/UAS-mCD8::GFP embryos (20h AEL±3). (f) Class I vpda neurons taken from 2-21gal4/UAS-mCD8::GFP, mhc1 mutant embryos (20h AEL±3). (g)

Quantification of the number of branches at each order of complexity (h) Quantification of the branch lengths at each order of complexity. For (g)and (h) Control (Blue) n=27 Mhc1 mutant (yellow) n=35. (i) Control Class I vpda neurons injected with water (j) Class I vpda neurons injected with Ryanodine. For (i) and (j) embryos were taken from homozygous 2-21gal4/UAS-mCD8::GFP (k) Quantification of the number of branches at each order of complexity. (l) Quantification of the branch lengths at each order of complexity. For (k) and (l) Water (blue) n=24 Ryanodine (yellow) n=31. For each box, the central line is the median, the 'o' is the mean, the box extends vertically between the 25th and 75th percentiles, the whiskers extend to the most extreme data that are not considered outliers, and the outliers are plotted individually. Statistical significance has been calculated using Mann-Whitney U test. ns, * p<0.05; ** p<0.01, *** p<0.001. All the panels have the same orientation: dorsal at the top, anterior to the left. Scale bars = 10μm.

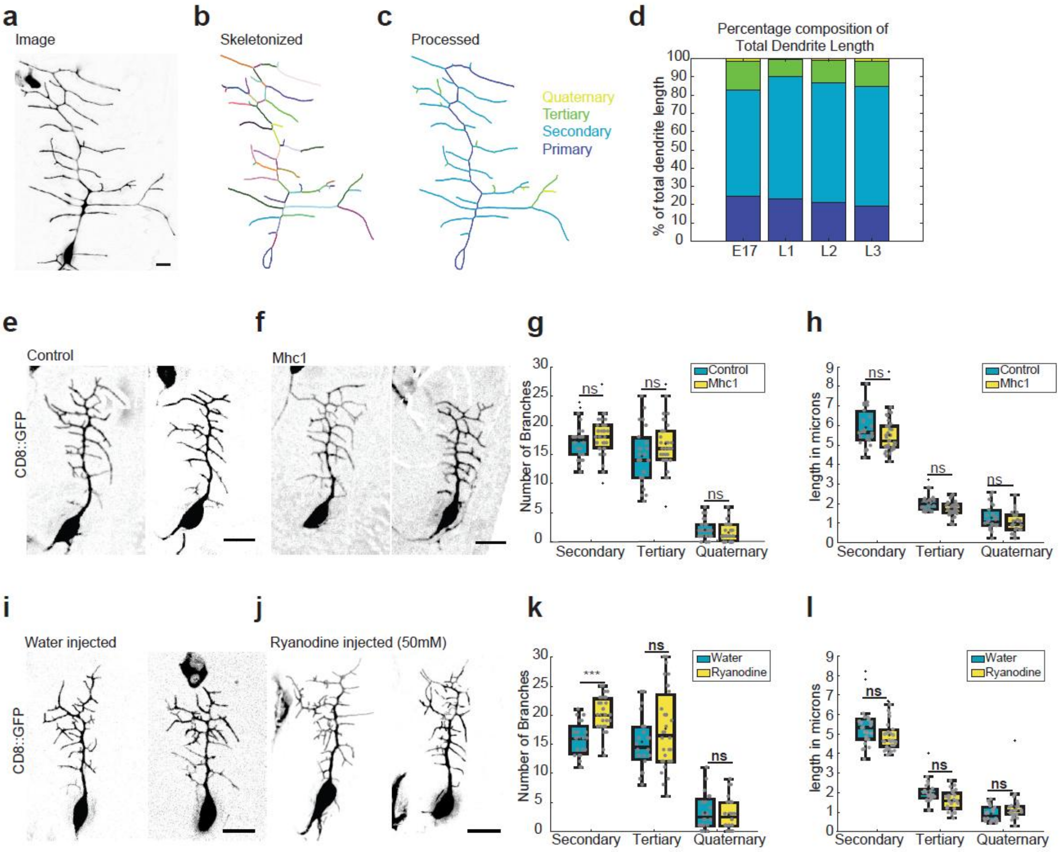

Figure S2. When the primary branch does not follow the stretched E-cadherin cell boundaries, it remains parallel to them

(a) Image of neuron at ~15h AEL co-imaged with Ecad::tomato. Inset: Close up of primary dendrite parallel to stretched E-cadherin cell boundaries as indicated by the white arrowheads. Scale bars = 10μm.

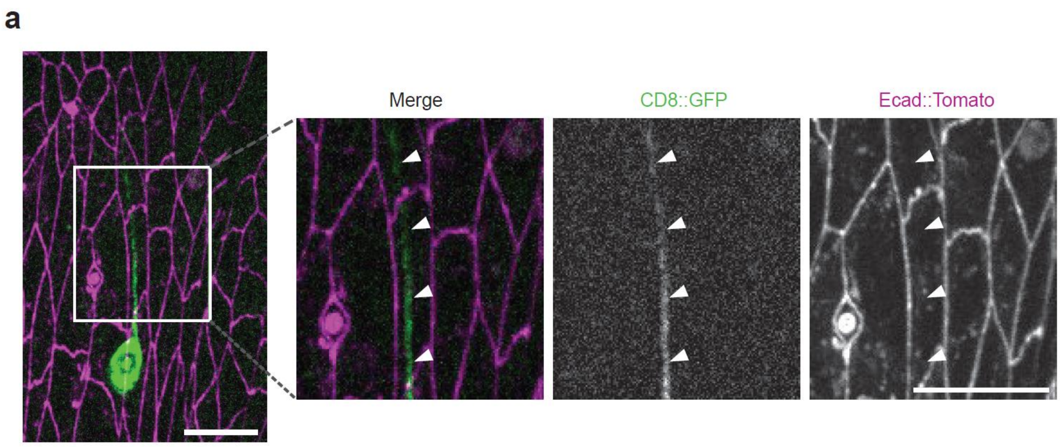

Figure S3. Difference between dendritic trees on abdominal segment A2 and A3
(a) Schematic: Larval filet (indicating vpda neurons in the abdominal hemi segments. Neurons in segment A2 and A3 on the left hemi-segment were used for analysis. Images of A2 (top panel) A3(bottom panel) vpda neurons at 96h AEL ±3 from homozygous 2-21gal4/UAS-mCD8::GFP larvae. The panel has the following orientation: Anterior at the top, Posterior at the bottom, ventral is the center and dorsal to the sides (b) Distribution of the total number of Secondary Branches n=42 (21 A2-A3 pairs). (c) Distribution of difference in number of Secondary branches between the A2-A3 pairs. (d) Secondary extensions do not shrink beyond forking points. Blue arrows indicate the forking point. (Movie7) Scale bars = 10μm.

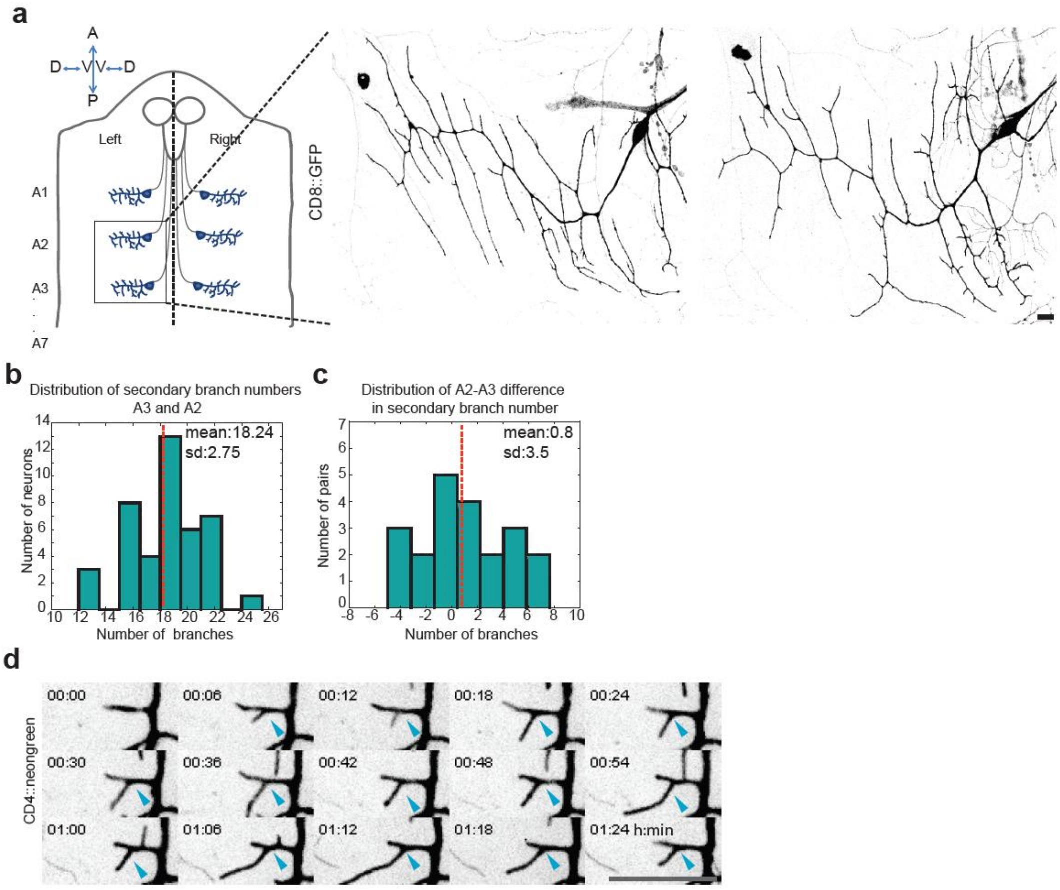

Figure S4. Computational Model for dendrite morphogenesis

(a) Diagram of dendritic morphologies at 25h AEL for different values of the ratio of spontaneous switching rates $r = k_{on}/k_{off}$ and branching rate of secondary branches $\lambda_{2,on}$. The values of the other computational parameters are fixed and defined in Table 1, Option 1. (b) Diagram of dendritic morphologies at 25h AEL for different values of the ratio of spontaneous switching rates $r = k_{on}/k_{off}$ and growth rate of secondary branches $v_{2,on}$. The growth rates of tertiary and quaternary branches are given by $v_{3/4,on} = v_{3/4,on}$ and the values of the other computational parameters are fixed and detailed in Table 1, Option 1. We again observe that the wide range of morphologies described by the model can be explored by varying the ratio r, as described in the Main Text for Fig. 4c. (c) and (d) Number of secondary branches over time from 16-25h AEL corresponding to the diagrams Fig. 4c (Main Text) and Fig S4a. In both figures, the growth rates for tertiary and quaternary branches are given by $v_{3/4,on} = v_{2,on}/2$ and the other computational values are fixed and given by Table 1, Option 1. (e) Number of secondary branches over time from 16-25h AEL obtained in simulations with the same values of the parameters and different aging protocols. By increasing the aging intensity we can explore different dendrite developments which range from structures with a large number of branches to situations where only a few secondary branches survive at the end. (f) Average length of secondary branches and (g) Average length of tertiary branches over time from 16-25h AEL. Both in (f) and (g) red lines represents simulations with the two different aging protocols AP1 (full line) and AP2 (dashed line) (Fig. 4d Main Text) and the boxes represent the experimental data. (h) Top: Number of Tertiary branches over time from 17-22h AEL for the computational models with (red) and without (green) self-repulsion using both aging protocols AP1 (full line) and AP2 (dashed line) described in Fig. 4d of the Main Text. Bottom: Average length of secondary branches over time from 16-22h AEL for the computational models with (red) and without (green) self-repulsion using both aging protocols AP1 (full line) and AP2 (dashed line) described in Fig. 4d of the Main Text. (i) Top: Number of secondary branches over time from 16-22h AEL for the computational models with self-repulsion and child branches (red) and with self-avoidance but no child extensions (blue) using AP2 (Fig. 4d Main Text). Bottom: Number of secondary branches over time from 16-22h AEL for the computational models with (red) and without (green) self-repulsion using AP2 (Fig. 4d Main Text). (j) Probability distribution of the angles between primary and secondary branches at 22h AEL. Red and green lines represent simulations with and without self-repulsion, respectively using AP2 (Fig. 4d Main Text). The number of simulations for all cases in (c) and (d) and (e) was $N_{sim} = 50$ while for all cases in (f), (g), (h), (i) and (j) it was $N_{sim} = 500$. In all figures, simulation lines represent the average value of the realizations and shadows represent the 1σ confidence interval. In addition, a 2-point time-averaging was performed using spline interpolation for lines in (f), (g), (h) and (i). For (e), AP1 in (f) and (g), and AP1 with and without self-repulsion in (h) the initial values of the computational parameters are detailed in Table 1, Option 1. For AP2 in (f) and (g), AP2 with and without self-repulsion in (h), and all cases in (i) and (j) the initial values of the computational parameters are detailed in Table 1, Option 2. For each box corresponding to *in vivo* observations, the central line is the median, the box extends vertically between the 25th and 75th percentiles and the whiskers extend to the most extreme data that are not considered outliers.

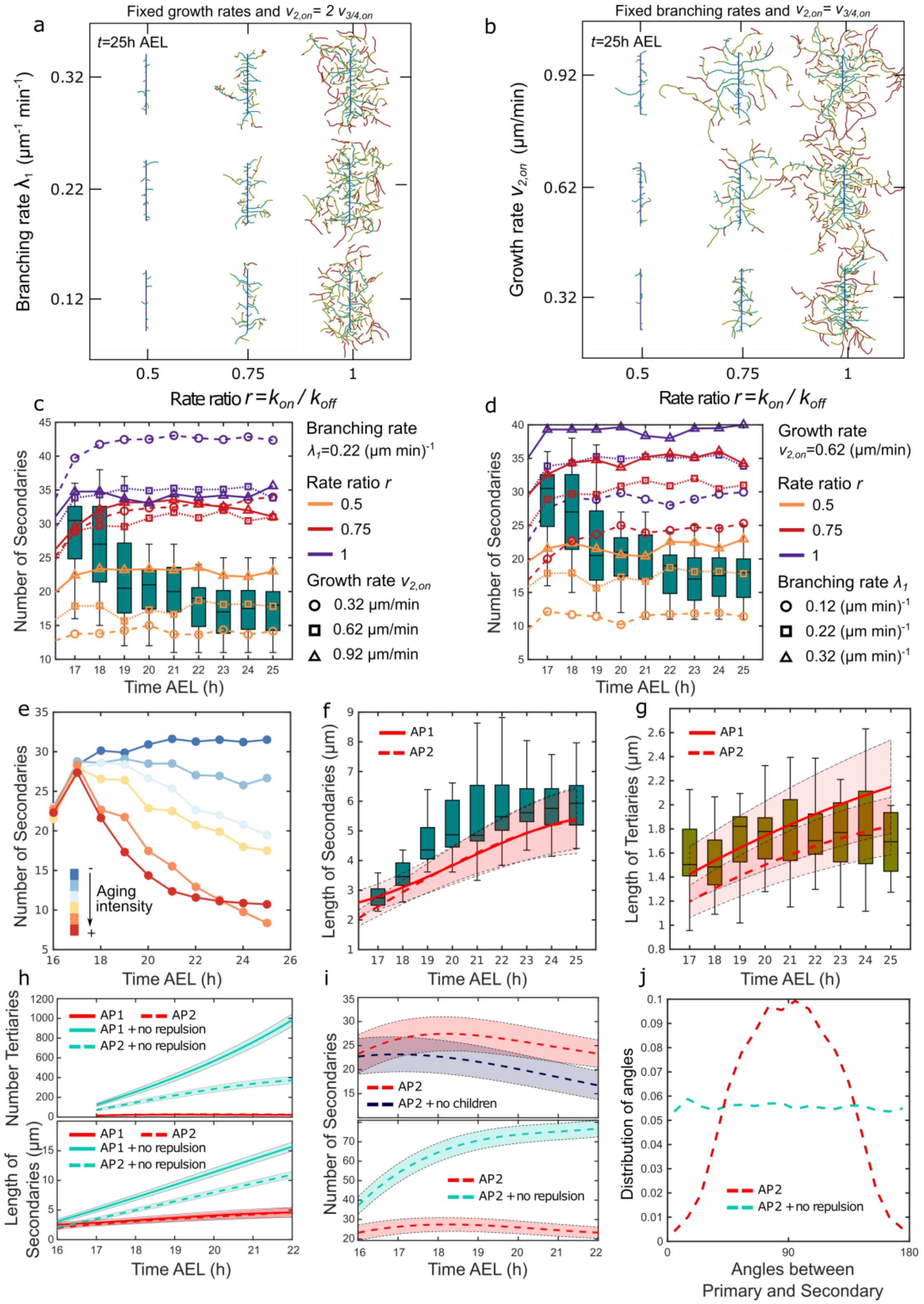

Figure S5. Secondary Branches require Dscam1 to allow a preferential orthogonal stabilization

(a) Left Panel: Control Class I vpda neurons taken from homozygous embryos of 2-21gal4/UAS-mCD4::neongreen. Right Panel: *dscam*^{P1} mutant neurons taken from embryos of *dscam*^{P1}/ΔDscam1;2-21gal4/UAS-mCD4::neongreen. Neurons imaged at ~15h AEL. (b) Quantification of Primary Branch lengths at ~22h AEL. (c) Schematic: Branches oriented outwards (Green arrows) Branches oriented in other directions (magenta arrows). Mean

Lengths of Secondary branches oriented orthogonally vs non-orthogonally. (d) Quantification of number of branches at each order of complexity. Schematic: Primary branch (blue) Secondary branches (cyan) Tertiary (brown) Quaternary (red). Control (blue) n=9 *dscam*^{P1} mutant (yellow) n=8. For each box, the central line is the median, the 'o' is the mean, the box extends vertically between the 25th and 75th percentiles, the whiskers extend to the most extreme data that are not considered outliers, and the outliers are plotted individually. Statistical significance has been calculated using Mann-Whitney U test. ns, * p<0.05; ** p<0.01, *** p<0.001. All the panels have the same orientation: dorsal at the top, anterior to the left. Scale bars = 10µm.

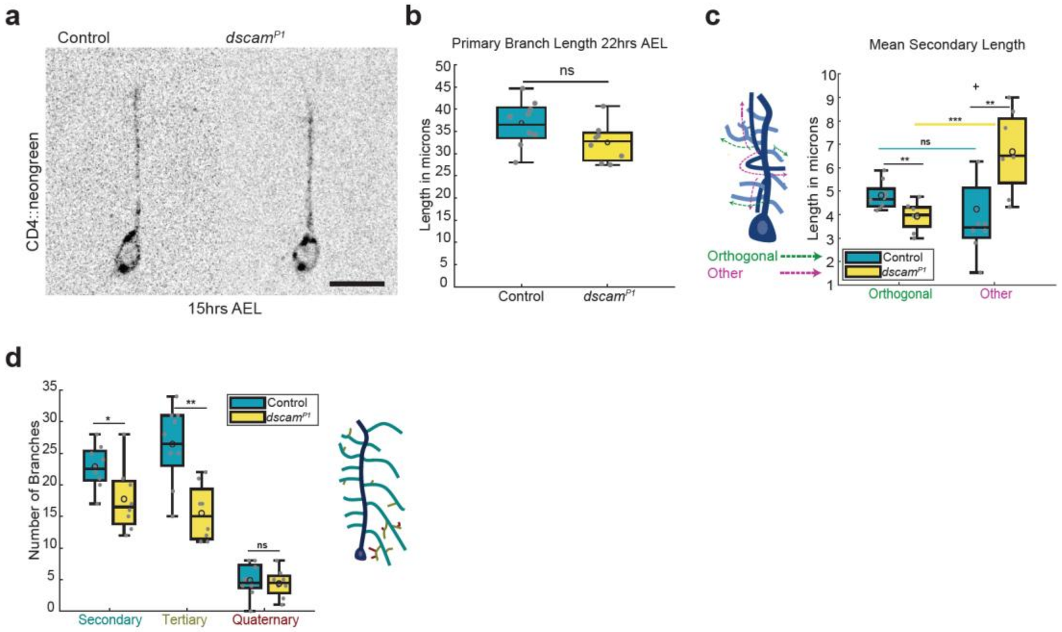

VIDEO

Video Legends

Video1: Time-lapse of embryonic development of the class I vpda neuron from ~16h to 25hrs AEL marked mCD8::GFP. Frame rate: 3min. Scale bars = 10µm. Related to Figure 1.

Video2: Time-lapse primary dendrite development from ~14h to 15h AEL marked mCD8::GFP. Frame rate: 3min. Scale bars = 10µm. Related to Figure 2.

Video3: Time-lapse of embryonic development of control and ablated neuron from ~16h to 25hrs AEL marked mCD8::GFP. Frame rate: 30min. Scale bars = 10µm. Related to Figure 2

Video4: Time-lapse of vpda neuron ~18h AEL marked mCD8::GFP. Frame rate: 30sec. Scale bars = 10µm. Related to Figure 3.

Video5: Simulation Video for two realizations for the parameter set defined in Table 1, Option 1 and aging protocol AP1. Primary branch (dark blue) has a constant length $L_1 =$ 30µm. Related to Figure 4.

Video6: Time-lapse of vpda neuron marked mCD8::GFP showing secondary dendrites do not retract beyond a forking point. Frame rate: 3min. Scale bars = 10µm. Related to Figure 4 and S2.

Video7: Time-lapse of control and *dscam*^{P1} vpda neuron development from ~17h-22h AEL marked mCD4::neongreen. Frame rate: 2min. Scale bars = 10µm. Related to Figure 5

Video8: Time-lapse of *dscam*^{P1} vpda neuron marked mCD4::neongreen showing remnant self-repulsion. Frame rate: 3min. Scale bars = 10µm. Related to Figure 5.

REFERENCES

1. Kulkarni, V.A., and Firestein, B.L. (2012). The dendritic tree and brain disorders. Mol. Cell. Neurosci. *50*, 10–20.
2. Scott, E.K., and Luo, L. (2001). How do dendrites take their shape? Nat. Neurosci. *4*, 359–365.
3. Hattori, Y., Usui, T., Satoh, D., Moriyama, S., Shimono, K., Itoh, T., Shirahige, K., and Uemura, T. (2013). Sensory-Neuron Subtype-Specific Transcriptional Programs Controlling Dendrite Morphogenesis: Genome-wide Analysis of Abrupt and Knot/Collier. Dev. Cell *27*, 530–544.
4. Smith, C.J., O'Brien, T., Chatzigeorgiou, M., Clay Spencer, W., Feingold-Link, E., Husson, S.J., Hori, S., Mitani, S., Gottschalk, A., Schafer, W.R., *et al.* (2013). Sensory neuron fates are distinguished by a transcriptional switch that regulates dendrite branch stabilization. Neuron *79*, 266–280.
5. Grueber, W.B., Jan, L.Y., and Jan, Y.N. (2003). Different levels of the homeodomain protein cut regulate distinct dendrite branching patterns of Drosophila multidendritic neurons. Cell *112*, 805–818.
6. Hattori, Y., Sugimura, K., and Uemura, T. (2007). Selective expression of Knot/Collier, a transcriptional regulator of the EBF/Olf-1 family, endows the Drosophila sensory system with neuronal class-specific elaborated dendritic patterns. Genes to Cells *12*, 1011–1022.
7. Sugimura, K., Satoh, D., Estes, P., Crews, S., and Uemura, T. (2004). Development of morphological diversity of dendrites in Drosophila by the BTB-zinc finger protein abrupt. Neuron *43*, 809–822.
8. Li, W., Wang, F., Menut, L., and Gao, F.B. (2004). BTB/POZ-zinc finger protein abrupt suppresses dendritic branching in a neuronal subtype-specific and dosage-dependent manner. Neuron *43*, 823–834.
9. Scott, E.K., Reuter, J.E., and Luo, L. (2003). Small GTPase Cdc42 is required for multiple aspects of dendritic morphogenesis. J. Neurosci. *23*, 3118–23.
10. Lee, A., Li, W., Xu, K., Bogert, B.A., Su, K., and Gao, F.B. (2003). Control of dendritic development by the Drosophila fragile X-related gene involves the small GTPase Rac1. Development *130*, 5543–5552.
11. Lee, T., Winter, C., Marticke, S.S., Lee, A., and Luo, L. (2000). Essential Roles of Drosophila RhoA in the Regulation of Neuroblast Proliferation and Dendritic but Not Axonal Morphogenesis. Neuron *25*, 307–316.
12. Nakayama, A.Y., Harms, M.B., and Luo, L. (2000). Small GTPases Rac and Rho in the Maintenance of Dendritic Spines and Branches in Hippocampal Pyramidal Neurons. J. Neurosci. *20*, 5329–5338.
13. Iyer, S.C., Wang, D., Iyer, E.P.R., Trunnell, S.A., Meduri, R., Shinwari, R., Sulkowski, M.J., and Cox, D.N. (2012). The RhoGEF Trio Functions in Sculpting Class Specific Dendrite Morphogenesis in Drosophila Sensory Neurons. PLoS One *7*, e33634.
14. Rosario, M., Schuster, S., Juttner, R., Parthasarathy, S., Tarabykin, V., and Birchmeier, W. (2012). Neocortical dendritic complexity is controlled during development by NOMA-GAP-dependent inhibition of Cdc42 and activation of cofilin. Genes Dev. *26*, 1743–1757.
15. Stürner, T., Tatarnikova, A., Mueller, J., Schaffran, B., Cuntz, H., Zhang, Y., Nemethova, M., Bogdan, S., Small, V., and Tavosanis, G. (2019). Transient

localization of the Arp2/3 complex initiates neuronal dendrite branching in vivo. Development *146*, dev171397.

16. Park, M., Salgado, J.M., Ostroff, L., Helton, T.D., Robinson, C.G., Harris, K.M., and Ehlers, M.D. (2006). Plasticity-Induced Growth of Dendritic Spines by Exocytic Trafficking from Recycling Endosomes. Neuron *52*, 817–830.
17. Zou, W., Yadav, S., DeVault, L., Jan, Y.N., and Sherwood, D.R. (2015). RAB-10-Dependent Membrane Transport Is Required for Dendrite Arborization. PLOS Genet. *11*, e1005484.
18. Satoh, D., Sato, D., Tsuyama, T., Saito, M., Ohkura, H., Rolls, M.M., Ishikawa, F., and Uemura, T. (2008). Spatial control of branching within dendritic arbors by dynein-dependent transport of Rab5-endosomes. Nat. Cell Biol. *10*, 1164–1171.
19. Ye, B., Zhang, Y., Song, W., Younger, S.H., Jan, L.Y., and Jan, Y.N. (2007). Growing Dendrites and Axons Differ in Their Reliance on the Secretory Pathway. Cell *130*, 717–729.
20. Cui-Wang, T., Hanus, C., Cui, T., Helton, T., Bourne, J., Watson, D., Harris, K.M., and Ehlers, M.D. (2012). Local Zones of Endoplasmic Reticulum Complexity Confine Cargo in Neuronal Dendrites. Cell *148*, 309–321.
21. Morita, A. (2006). Regulation of Dendritic Branching and Spine Maturation by Semaphorin3A-Fyn Signaling. J. Neurosci. *26*, 2971–2980.
22. Furrer, M.-P., Vasenkova, I., Kamiyama, D., Rosado, Y., and Chiba, A. (2007). Slit and Robo control the development of dendrites in Drosophila CNS. Development *134*, 3795–3804.
23. Whitford, K.L., Dijkhuizen, P., Polleux, F., and Ghosh, A. (2002). Molecular Control of Cortical Dendrite Development. Annu. Rev. Neurosci. *25*, 127–149.
24. Dimitrova, S., Reissaus, A., and Tavosanis, G. (2008). Slit and Robo regulate dendrite branching and elongation of space-filling neurons in Drosophila. Dev. Biol. *324*, 18–30.
25. Matthews, B.J., and Grueber, W.B. (2011). Dscam1-Mediated Self-Avoidance Counters Netrin-Dependent Targeting of Dendrites in Drosophila. Curr. Biol. *21*, 1480–1487.
26. Furrer, M.-P., Kim, S., Wolf, B., and Chiba, A. (2003). Robo and Frazzled/DCC mediate dendritic guidance at the CNS midline. Nat. Neurosci. *6*, 223–230.
27. Teichmann, H.M., and Shen, K. (2011). UNC-6 and UNC-40 promote dendritic growth through PAR-4 in Caenorhabditis elegans neurons. Nat. Neurosci. *14*, 165–172.
28. Dong, X., Liu, O.W., Howell, A.S., and Shen, K. (2013). An extracellular adhesion molecule complex patterns dendritic branching and morphogenesis. Cell *155*, 296–307.
29. Lanoue, V., Usardi, A., Sigoillot, S.M., Talleur, M., Iyer, K., Mariani, J., Isope, P., Vodjdani, G., Heintz, N., and Selimi, F. (2013). The adhesion-GPCR BAI3, a gene linked to psychiatric disorders, regulates dendrite morphogenesis in neurons. Mol. Psychiatry *18*, 943–950.
30. Han, C., Wang, D., Soba, P., Zhu, S., Lin, X., Jan, L.Y., and Jan, Y.N. (2012). Integrins Regulate Repulsion-Mediated Dendritic Patterning of Drosophila Sensory Neurons by Restricting Dendrites in a 2D Space. Neuron *73*, 64–78.
31. Gaudillière, B., Konishi, Y., De La Iglesia, N., Yao, G.L., and Bonni, A. (2004). A CaMKII-NeuroD Signaling Pathway Specifies Dendritic Morphogenesis. Neuron *41*, 229–241.
32. Puram, S. V., Kim, A.H., Ikeuchi, Y., Wilson-Grady, J.T., Merdes, A., Gygi, S.P., and Bonni, A. (2011). A CaMKIIβ signaling pathway at the centrosome regulates dendrite patterning in the brain. Nat. Neurosci. *14*, 973–983.
33. Wang, S., Sekiguchi, R., Daley, W.P., and Yamada, K.M. (2017). Patterned cell and matrix dynamics in branching morphogenesis. J. Cell Biol. *216*, 559–570.
34. Hannezo, E., Scheele, C.L.G.J., Moad, M., Drogo, N., Heer, R., Sampogna, R. V., van Rheenen, J., and Simons, B.D. (2017). A Unifying Theory of Branching

Morphogenesis. Cell *171*, 242-255.e27.

35. Metzger, Ross J., Krasow, M.A. (1999). Genetic control of Branching Morphogenesis. Science (80-.). *284*, 1635–1639.
36. Metzger, R.J., Klein, O.D., Martin, G.R., and Krasnow, M.A. (2008). The Branching Program of Mouse Lung Development. Nature *453*, 745–750.
37. Samakovlis, C., Hacohen, N., Manning, G., Sutherland, D.C., Guillemin, K., and Krasnow, M.A. (1996). Development of the Drosophila tracheal system occurs by a series of morphologically distinct but genetically coupled branching events. Development *122*, 1395–1407.
38. Salzberg, Y., Díaz-Balzac, C.A., Ramirez-Suarez, N.J., Attreed, M., Tecle, E., Desbois, M., Kaprielian, Z., and Bülow, H.E. (2013). Skin-derived cues control arborization of sensory dendrites in Caenorhabditis elegans. Cell *155*, 308.
39. Zou, W., Shen, A., Dong, X., Tugizova, M., Xiang, Y.K., and Shen, K. (2016). A multi-protein receptor-ligand complex underlies combinatorial dendrite guidance choices in C. elegans. Elife *5*, 1–25.
40. Díaz-Balzac, C.A., Rahman, M., Lázaro-Peña, M.I., Martin Hernandez, L.A., Salzberg, Y., Aguirre-Chen, C., Kaprielian, Z., and Bülow, H.E. (2016). Muscle- and Skin-Derived Cues Jointly Orchestrate Patterning of Somatosensory Dendrites. Curr. Biol. *26*, 2379–2387.
41. Ochoa-espinosa, A., and Affolter, M. (2012). Branching Morphogenesis from Cells to Organs and Back. Cold Spring Harb Perspect Biol. *4*, 1–14.
42. Gjorevski, N., and Nelson, C.M. (2011). Integrated morphodynamic signalling of the mammary gland. Nat. Rev. Mol. Cell Biol. *12*, 581–593.
43. Campos-Ortega, J.A. (1997). Asymmetric division: Dynastic intricacies of neuroblast division. Curr. Biol. *7*, 726–728.
44. Freeman, M. (1996). Reiterative Use of the EGF Receptor Triggers Differentiation of All Cell Types in the Drosophila Eye. Cell *87*, 651–660.
45. Changeux, J.-P., and Danchin, A. (1976). Selective stabilisation of developing synapses as a mechanism for the specification of neuronal networks. Nature *264*, 705–712.
46. Macagno, E.R., Lopresti, V., and Levinthal, C. (1973). Structure and Development of Neuronal Connections in Isogenic Organisms: Variations and Similarities in the Optic System of Daphnia magna. Proc. Natl. Acad. Sci. *70*, 57–61.
47. Goodman, C.S., Pearson, K.G., and Heitler, W.J. (1979). Variability of identified neurons in grasshoppers. Comp. Biochem. Physiol. Part A Physiol. *64*, 455–462.
48. Bodmer, R., and Jan, Y.N. (1987). Morphological differentiation of the embryonic peripheral neurons in Drosophila. Rouxs Arch. Dev. Biol. *196*, 69–77.
49. Grueber, W.B., Ye, B., Moore, A.W., Jan, L.Y., and Jan, Y.N. (2003). Dendrites of Distinct Classes of Drosophila Sensory Neurons Show Different Capacities for Homotypic Repulsion. Curr. Biol. *13*, 618–626.
50. Grueber, W.B., Jan, L.Y., and Jan, Y.N. (2002). Tiling of the Drosophila epidermis by multidendritic sensory neurons. Development *129*, 2867–2878.
51. Gao, F.B., Kohwi, M., Brenman, J.E., Jan, L.Y., and Jan, Y.N. (2000). Control of dendritic field formation in Drosophila: the roles of flamingo and competition between homologous neurons. Neuron *28*, 91–101.
52. Iyer, E.P.R., Iyer, S.C., Sullivan, L., Wang, D., Meduri, R., Graybeal, L.L., and Cox, D.N. (2013). Functional Genomic Analyses of Two Morphologically Distinct Classes of Drosophila Sensory Neurons: Post-Mitotic Roles of Transcription Factors in Dendritic Patterning. PLoS One *8*, e72434.
53. Parrish, J.Z., Xu, P., Kim, C.C., Jan, L.Y., and Jan, Y.N. (2009). The microRNA bantam Functions in Epithelial Cells to Regulate Scaling Growth of Dendrite Arbors in Drosophila Sensory Neurons. Neuron *63*, 788–802.
54. Shimono, K., Fujishima, K., Nomura, T., Ohashi, M., Usui, T., Kengaku, M., Toyoda, A., and Uemura, T. (2015). An evolutionarily conserved protein CHORD regulates scaling of dendritic arbors with body size. Sci. Rep. *4*, 4415.

55. Schmucker, D., J.C., C., H., S., C.A., W., J., X., M., M., J.E., D., and S.L., Z. (2000). Drosophila Dscam is an axon guidance receptor exhibiting extraordinary molecular diversity. Cell *101*, 671–684.
56. Soba, P., Zhu, S., Emoto, K., Younger, S., Yang, S.J., Yu, H.H., Lee, T., Jan, L.Y., and Jan, Y.N. (2007). Drosophila Sensory Neurons Require Dscam for Dendritic Self-Avoidance and Proper Dendritic Field Organization. Neuron *54*, 403–416.
57. Matthews, B.J., Kim, M.E., Flanagan, J.J., Hattori, D., Clemens, J.C., Zipursky, S.L., and Grueber, W.B. (2007). Dendrite Self-Avoidance Is Controlled by Dscam. Cell *129*, 593–604.
58. Hughes, M.E., Bortnick, R., Tsubouchi, A., Bäumer, P., Kondo, M., Uemura, T., and Schmucker, D. (2007). Homophilic Dscam Interactions Control Complex Dendrite Morphogenesis. Neuron *54*, 417–427.
59. Menon, S., and Gupton, S. (2018). Recent advances in branching mechanisms underlying neuronal morphogenesis. F1000Research *7*, 1–12.
60. Singhania, A., and Grueber, W.B. (2014). Development of the embryonic and larval peripheral nervous system of Drosophila. Wiley Interdiscip. Rev. Dev. Biol. *3*, 193–210.
61. Jan, Y.-N., and Jan, L.Y. (2010). Branching out: mechanisms of dendritic arborization. Nat. Rev. Neurosci. *11*, 316–328.
62. Gao, F.B., Brenman, J.E., Jan, L.Y., and Jan, Y.N. (1999). Genes regulating dendritic outgrowth, branching, and routing in Drosophila. Genes Dev. *13*, 2549–2561.
63. Dong, X., Shen, K., and Bülow, H.E. (2015). Intrinsic and Extrinsic Mechanisms of Dendritic Morphogenesis. Annu. Rev. Physiol. *77*, 271–300.
64. Sugimura, K., Yamamoto, M., Niwa, R., Satoh, D., Goto, S., Taniguchi, M., Hayashi, S., and Uemura, T. (2003). Distinct developmental modes and lesion-induced reactions of dendrites of two classes of Drosophila sensory neurons. J. Neurosci. *23*, 3752–3760.
65. Komiyama, T., Sweeney, L.B., Schuldiner, O., Garcia, K.C., and Luo, L. (2007). Graded Expression of Semaphorin-1a Cell-Autonomously Directs Dendritic Targeting of Olfactory Projection Neurons. Cell *128*, 399–410.
66. Shen, H.-C., Chu, S.-Y., Hsu, T.-C., Wang, C.-H., Lin, I.-Y., and Yu, H.-H. (2017). Semaphorin-1a prevents Drosophila olfactory projection neuron dendrites from mis-targeting into select antennal lobe regions. PLOS Genet. *13*, e1006751.
67. Lawlor, K.T., Ly, D.C., and DiNardo, S. (2013). Drosophila Dachsous and Fat polarize actin-based protrusions over a restricted domain of the embryonic denticle field. Dev. Biol. *383*, 285–294.
68. Franze, K. (2020). Integrating Chemistry and Mechanics: The Forces Driving Axon Growth. Annu. Rev. Cell Dev. Biol. *36*, annurev-cellbio-100818-125157.
69. Puram, S. V., and Bonni, A. (2013). Cell-intrinsic drivers of dendrite morphogenesis. Dev. *140*, 4657–4671.
70. Castro, A.F., Baltruschat, L., Stürner, T., Bahrami, A., Jedlicka, P., Tavosanis, G., and Cuntz, H. (2020). Achieving functional neuronal dendrite structure through sequential stochastic growth and retraction. Biorixiv. doi: https://doi.org/10.1101/2020.07.09.195446
71. Matsubara, D., Horiuchi, S.Y., Shimono, K., Usui, T., and Uemura, T. (2011). The seven-pass transmembrane cadherin Flamingo controls dendritic self-avoidance via its binding to a LIM domain protein, Espinas, in Drosophila sensory neurons. Genes Dev. *25*, 1982–1996.
72. Liao, C.P., Li, H., Lee, H.H., Chien, C.T., and Pan, C.L. (2018). Cell-Autonomous Regulation of Dendrite Self-Avoidance by the Wnt Secretory Factor MIG-14/Wntless. Neuron *98*, 320-334.e6.
73. Long, H., Ou, Y., Rao, Y., and van Meyel, D.J. (2009). Dendrite branching and self-avoidance are controlled by Turtle, a conserved IgSF protein in Drosophila. Development *136*, 3475–3484.
74. Hattori, Y., Usui, T., Satoh, D., Moriyama, S., Shimono, K., Itoh, T., Shirahige, K.,

and Uemura, T. (2013). Sensory-Neuron Subtype-Specific Transcriptional Programs Controlling Dendrite Morphogenesis: Genome-wide Analysis of Abrupt and Knot/Collier. Dev. Cell *27*, 530–544.

75. Parrish, J.Z., Kim, M.D., Lily, Y.J., and Yuh, N.J. (2006). Genome-wide analyses identify transcription factors required for proper morphogenesis of Drosophila sensory neuron dendrites. Genes Dev. *20*, 820–835.
76. O'Donnell, P.T., and Bernstein, S.I. (1988). Molecular and ultrastructural defects in a Drosophila myosin heavy chain mutant: differential effects on muscle function produced by similar thick filament abnormalities. J. Cell Biol. *107*, 2601–2612.
77. Yu, D., Baird, M.A., Allen, J.R., Howe, E.S., Klassen, M.P., Reade, A., Makhijani, K., Song, Y., Liu, S., Murthy, Z., *et al.* (2015). A naturally monomeric infrared fluorescent protein for protein labeling in vivo. Nat. Methods *12*, 763–765.
78. Schindelin, J., Arganda-Carreras, I., Frise, E., Kaynig, V., Longair, M., Pietzsch, T., Preibisch, S., Rueden, C., Saalfeld, S., Schmid, B., *et al.* (2012). Fiji: an open-source platform for biological-image analysis. Nat. Methods *9*, 676–682.
79. Li, W., and Gao, F.-B. (2003). Actin filament-stabilizing protein tropomyosin regulates the size of dendritic fields. J. Neurosci. *23*, 6171–6175.
80. Pilot, F., Philippe, J.M., Lemmers, C., Chauvin, J.P., and Lecuit, T. (2006). Developmental control of nuclear morphogenesis and anchoring by charleston, identified in a functional genomic screen of Drosophila cellularisation. Development *133*, 711–723.
81. Parton, R.M., Valles, A.M., Dobbie, I.M., and Davis, I. (2010). Drosophila Larval Fillet Preparation and Imaging of Neurons. Cold Spring Harb. Protoc. *2010*, pdb.prot5405-pdb.prot5405.
82. Gittes, F., Mickey, B., Nettleton, J., and Howard, J. (1993). Flexural rigidity of microtubules and actin filaments measured from thermal fluctuations in shape. J. Cell Biol. *120*, 923–934.